Received: 15 February 2024 | Revised: 8 July 2024 | Accepted: 29 July 2024

DOI: 10.1002/qj.4839

Quarterly Journal of the Royal Meteorological Society RMetS

RESEARCH ARTICLE

Robust and accurate simulations of flows over orography using non-conforming meshes

Giuseppe Orlando[1] | **Tommaso Benacchio**[2] | **Luca Bonaventura**[3]

[1]CMAP, CNRS, École Polytechnique, Institute Polytechnique de Paris, Palaiseau, France

[2]Weather Research, Danish Meteorological Institute, Copenhagen, Denmark

[3]Dipartimento di Matematica, Politecnico di Milano, Milan, Italy

Correspondence
Luca Bonaventura, Dipartimento di Matematica, Politecnico di Milano, Piazza Leonardo da Vinci 32, 20133 Milano, Italy.
Email: luca.bonaventura@polimi.it

Funding information
ESCAPE-2, European Union EXCELLENT SCIENCE - Future and Emerging Technologies (FET) programme, Grant/Award Number: 800897

Abstract
We systematically validate the static local mesh refinement capabilities of a recently proposed implicit–explicit discontinuous Galerkin scheme implemented in the framework of the deal.II library. Non-conforming meshes are employed in atmospheric flow simulations to increase the resolution around complex orography. The proposed approach is fully mass and energy conservative and allows local mesh refinement in the vertical and horizontal direction without relaxation at the internal coarse/fine mesh boundaries. A number of numerical experiments based on classical benchmarks with idealized as well as more realistic orography profiles demonstrate that simulations with the locally refined mesh are stable for long lead times and that no spurious effects arise at the interfaces of mesh regions with different resolutions. Moreover, correct values of the momentum flux are retrieved and the correct large-scale orographic response is reproduced. Hence, large-scale orography-driven flow features can be simulated without loss of accuracy using a much lower total amount of degrees of freedom.

KEYWORDS
discontinuous Galerkin methods, flows over orography, lee waves, non-conforming meshes, numerical weather prediction

1 | INTRODUCTION

Atmospheric flows display phenomena on a very wide range of spatial scales that interact with each other. Many strongly localized features, such as complex orography or hurricanes, can only be modelled correctly if a very high spatial resolution is employed, especially in the lower troposphere, whereas larger scale features such as high-/low-pressure systems and stratospheric flows can be adequately resolved on much coarser meshes. The impact of orography on the atmospheric circulation has been the focus of a large number of studies; for example, see the classical work of McFarlane (1987) and the more recent review by Sandu *et al.* (2019), and references therein. This impact is significant both on the short and long time-scales and even affects the oceanic circulation (Maffre *et al.* 2018). The minimal resolution requirements for an accurate description of the atmospheric phenomena relevant for numerical weather prediction (NWP) and climate models have been subject to strong debate; for example, see the classical paper by Lindzen and Fox-Rabinovitz (1989) and the more recent contribution by Skamarock *et al.* (2019), and the references therein. Furthermore, for numerical reasons, orography data used by NWP and climate models are often filtered, thus limiting the scales at which orography can effectively be represented in numerical models. For example, the analysis in Davies and Brown (2001) showed that orographic features must be resolved by a sufficiently large number of mesh points (from six to ten) in finite-difference models to avoid spurious numerical features.

The insufficient resolution of orographic features is compensated in NWP and climate models by subgrid-scale orographic drag parametrizations (Miller *et al.* 1989; Palmer *et al.* 1986), which are essential for an accurate description of atmospheric flows with models using feasible resolutions; see again the discussion in Sandu *et al.* (2019). The interplay between resolved and parametrized orographic effects is critical, since many operational models currently employ resolutions in the so-called "grey zone", for which some orographic effects are well resolved whereas others still require parametrization. Global simulations with the European Centre of Medium-range Weather Forecasts' Integrated Forecasting System NWP model without drag parametrization showed that the increase in forecast skill for increasing atmospheric resolution was chiefly due to the improved representation of the orography (Kanehama *et al.* 2019). When parametrizing the drag, the positive impact of the parametrization decreased as long as the model resolution increased. Finally, sharper orography representations also proved beneficial for simulations of mountain-wave-driven middle-atmosphere processes (Fritts *et al.* 2022).

Because of the multiscale nature of the underlying processes, NWP is an apparently ideal application area for adaptive numerical approaches. However, mesh adaptation strategies have only slowly found their way into the NWP literature, due to limitations of earlier numerical methods, concerns about the accuracy of variable-resolution meshes for the correct representation of typical atmospheric wave phenomena, and the greater complexity of an efficient parallel implementation for non-uniform or adaptive meshes. The first approaches to variable local mesh refinement were based on the nesting concept e.g. Harrison and Elsberry (1972); Phillips and Shukla (1973); Zhang *et al.* (1986). Early attempts to introduce adaptive meshes in NWP were then presented in the seminal papers of Skamarock *et al.* (1989); Skamarock and Klemp (1993), and a review of earlier variable-resolution approaches is presented in Côté (1997). The impact of variable-resolution meshes on classical finite-difference methods was analysed in Long and Thuburn (2011); Vichnevetsky (1987). More recently, methods allowing mesh deformation strategies were proposed in Prusa and Smolarkiewicz (2003), and techniques to estimate the required resolution were presented in Weller (2009), whereas applications of block structured meshes were discussed in Jablonowski *et al.* (2009). In all those articles, finite-difference or finite-volume methods were employed for the numerical approximation. High-order finite-element methods have also been exploited as an ingredient of accurate adaptive methods. More specifically, hybrid continuous–discontinuous finite-element techniques were employed in Li *et al.* (2021). Discontinuous Galerkin (DG) finite-element *h*-adaptive approaches were proposed in Kopera and Giraldo (2014); Müller *et al.* (2013); Yelash *et al.* (2014), and *p*-adaptive DG methods for NWP were introduced in Tumolo and Bonaventura (2015). An *hp*-adaptive DG method for mesoscale atmospheric modelling was recently proposed in Dolejsi (2024), and a fully unstructured three-dimensional (3D) approach was presented in Tissaoui *et al.* (2023). Finally, Düben and Korn (2014) investigated the impact of mesh refinement on large-scale geostrophic equilibrium and turbulent cascades influenced by the Earth's rotation.

Operational or semi-operational NWP models exist that have local mesh refinement (Skamarock *et al.* 2012) or nesting (Skamarock *et al.* 2021) capabilities. Almost all the published results, however, either require some relaxation at the boundaries between coarse and fine regions (McTaggart-Cowan *et al.* 2011; Tang *et al.* 2013) or perform vertical mesh refinement over the whole vertical span of the computational domain (Daniels *et al.* 2016; Mahalov and Moustaoui 2009; Mirocha and Lundquist 2017). A full 3D nesting approach without boundary relaxation is presented in Hellsten *et al.* (2021), which is only tested on cases either without orography or without stratification, with additional restrictions on the lateral boundary conditions that can be applied in the case of purely vertical nesting.

In this work, we test a recently proposed adaptive IMEX-DG method (Orlando 2023; Orlando *et al.* 2022, 2023) on a number of benchmarks for atmospheric flow over idealized and real orography. The proposed approach is fully mass and energy conservative and allows local mesh refinement in the vertical and horizontal direction without the need to apply relaxation at the internal coarse/fine mesh boundaries. Through a quantitative assessment of non-conforming *h*-adaptation, we aim to show that simulations with adaptive meshes around orography can increase the accuracy of the local flow description without affecting the larger scales, thereby significantly reducing the overall number of degrees of freedom compared with uniform mesh simulations. The numerical approach employed combines accurate and flexible DG space discretization with an implicit–explicit (IMEX) time discretization, whose properties and theoretical justifications are discussed in detail by Orlando and co-workers (Orlando, 2023), (Orlando *et al.* 2022, 2023). The adaptive discretization is implemented in the framework of the open-source numerical library deal.II (Arndt *et al.* 2023; Bangerth *et al.* 2007), which provides the non-conforming *h*-refinement capabilities exploited in the numerical simulation of flows over orography. The numerical results show that simulations with the refined meshes provide stable solutions with greater or comparable accuracy to those obtained with the uniform mesh. Importantly, no spurious reflections arise at internal boundaries separating mesh regions with different resolution, and correct values for the vertical flux of horizontal momentum are retrieved. Both on idealized benchmarks and on test cases over realistic orographic profiles, simulations using non-conforming local mesh refinement correctly reproduce the larger scale, far-field orographic response, with meshes that are relatively coarse over most of the domain. This supports the idea that locally refined, non-conforming meshes can be an effective tool to reduce the dependence of NWP and climate models on parametrizations of orographic effects (Kanehama *et al.* 2019; Sandu *et al.* 2019).

This article is structured as follows. The model equations and a short introduction to non-conforming meshes are presented in Section 2. The quantitative numerical assessment of non-conforming mesh refinement over orography in a number of idealized and real benchmarks is reported in Section 3. Some conclusions and considerations about open issues and future work are presented in Section 4.

2 | THE MODEL EQUATIONS

The fully compressible Euler equations of gas dynamics represent the most comprehensive mathematical model for atmosphere dynamics e.g. Davies *et al.* (2003); Giraldo and Restelli (2008); Steppeler *et al.* (2003). Let $\Omega \subset \mathbb{R}^d$, $2 \leq d \leq 3$ be a simulation domain and denote by $\mathbf{x}$ the spatial coordinates and by t the temporal coordinate. We consider the unsteady compressible Euler equations, written in conservation form as

$$\begin{aligned} \frac{\partial \rho}{\partial t} + \nabla \cdot (\rho \mathbf{u}) &= 0, \\ \frac{\partial (\rho \mathbf{u})}{\partial t} + \nabla \cdot (\rho \mathbf{u} \otimes \mathbf{u}) + \nabla p &= \rho \mathbf{g}, \\ \frac{\partial (\rho E)}{\partial t} + \nabla \cdot [(\rho E + p)\mathbf{u}] &= \rho \mathbf{g} \cdot \mathbf{u}, \end{aligned} \tag{1}$$

for $\mathbf{x} \in \Omega$, $t \in (0, T_{\mathrm{f}}]$, supplied with suitable initial and boundary conditions. Here, T_{f} is the final time, ρ is the density, $\mathbf{u}$ is the fluid velocity, p is the pressure, and $\otimes$ denotes the tensor product. Moreover, $\mathbf{g} = -g\mathbf{k}$ represents the acceleration of gravity, with $g = 9.81\ \mathrm{m \cdot s^{-2}}$ and $\mathbf{k}$ denoting the upward-pointing unit vector in the standard Cartesian frame of reference. The total energy ρE can be rewritten as $\rho E = \rho e + \rho k$, where e is the internal energy and $k = \frac{1}{2}\|\mathbf{u}\|^2$ is the kinetic energy. We also introduce the specific enthalpy $h = e + (p/\rho)$ and we notice that one can rewrite the energy flux as

$$(\rho E + p)\mathbf{u} = \left(e + k + \frac{p}{\rho}\right)\rho \mathbf{u} = (h + k)\rho \mathbf{u}.$$

Notice that the choice of the total energy density E as prognostic variable has been shown, at least empirically, to yield model formulations that do not require special well-balancing techniques for flows under the action of gravity (Baldauf and Pril (2023)). The aforementioned equations are complemented by the equation of state for ideal gases, given by $p = \rho R T$, with R being the specific gas constant. For later reference, we define the Exner pressure Π as

$$\Pi = \left(\frac{p_0}{p}\right)^{(\gamma-1)/\gamma}, \tag{2}$$

with $p_0 = 10^5$ Pa being a reference a pressure and γ denoting the isentropic exponent. We consider $\gamma = 1.4$ and the gas constant $R = 287\ \mathrm{J \cdot kg^{-1} \cdot K^{-1}}$ for all the test cases.

2.1 | Non-conforming meshes

We solve the system in Equation (1) numerically using the IMEX-DG solver proposed in Orlando (2023); Orlando *et al.* (2022) and validated in Orlando *et al.* (2023) for atmospheric applications; also see Orlando *et al.* (2024). Although, on the one hand, no special well-balancing property with respect to hydrostatic equilibrium has been proven for the proposed discretization—for example, see the proposal in Blaise *et al.* (2016)—no evidence of numerical problems related to the representation of hydrostatic equilibrium was found in the many numerical tests performed in the previously mentioned articles. This could be related to the choice of the energy density as prognostic variable, as argued in Baldauf and Pril (2023), based on numerical results obtained with a similar formulation.

Atmospheric flows such as those considered in this work are characterized by low Mach numbers, as motions of interest have characteristic speeds much lower than that of sound. In the low Mach limit, terms related to pressure gradients yield stiff components in the system of ordinary differential equations resulting from the spatial discretization of the system in Equation (1). Therefore, an implicit coupling between the momentum balance and the energy balance is adequate, whereas the density can be treated in a fully explicit fashion; for example, see the discussion in Casulli and Greenspan (1984); Dumbser and Casulli (2016). The time discretization is based on a variant of the IMEX method proposed in Giraldo *et al.* (2013), whereas the space discretization adopts the DG scheme implemented in the deal.II library (Arndt *et al.* 2023) for a complete analysis and discussion of the numerical methodology, and to Giraldo (2020) for a comprehensive introduction to the DG method.

The nodal DG method, as the one employed in deal.II (Arndt *et al.* 2023), is characterized by integrals over faces belonging to two elements. Moreover, a weak imposition of boundary conditions is typically adopted (Arnold *et al.* 2002). Hence, the method provides a natural framework for formulations on multiblock meshes. Consider a generic nonlinear conservation law

$$\frac{\partial \Psi}{\partial t} + \nabla \cdot \mathbf{F}(\Psi) = 0. \tag{3}$$

We multiply the previous relation by a test function Λ and, after integration by parts, we obtain the following local formulation on each element K of the mesh with boundary ∂K:

$$\int_K \frac{\partial \Psi}{\partial t}\Lambda \, d\Omega - \int_K \mathbf{F}(\Psi) \cdot \nabla\Lambda \, d\Omega + \int_{\partial K} \hat{\mathbf{F}}(\Psi^+, \Psi^-)\Lambda \, d\Sigma = 0, \tag{4}$$

where $d\Omega$ is the volume element and $d\Sigma$ is the surface element. In the surface integral, we replace the term $\mathbf{F}(\Psi)$ with a numerical flux $\hat{\mathbf{F}}(\Psi^+, \Psi^-)$, which depends on the solution on both sides Ψ^+ and Ψ^- of an interior face.

A non-conforming mesh is characterized by cells with different refinement levels, so that the resolution between two neighbouring cells can be different (Figure 1). For faces between cells of different refinement level, the integration is performed from the refined side and a suitable interpolation is performed on the coarse side, so as to guarantee the conservation property; see the discussion in Bangerth *et al.* (2007). Hence, no hanging nodes appear in the implementation of the discrete weak form of the equations.

DG methods with non-conforming meshes have been developed for different applications; for example, see Fahs (2015); Heinz *et al.* (2023). The main constraint posed by the deal.II library for the use of non-conforming meshes is the requirement of not having neighbouring cells with refinement levels differing by more than one. Thus, for each non-conforming face, flux contributions have to be considered at most from two refined faces in two dimensions and from four faces in three dimensions (Figure 1). The out-of-the-box availability in deal.II provides an ideal test bed for evaluating the potential computational savings using non-conforming meshes instead of uniform meshes in atmospheric flow simulations.

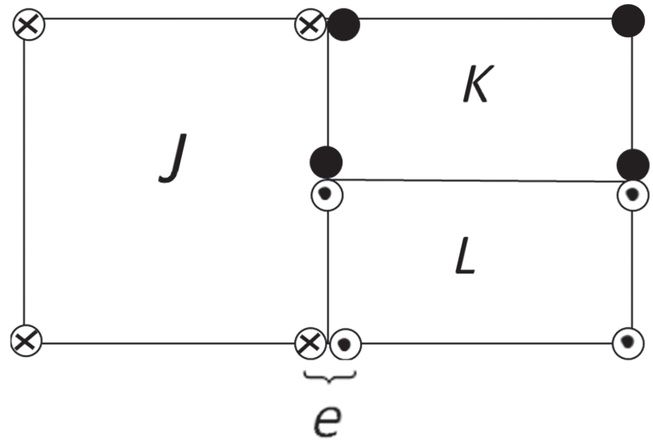

FIGURE 1 Example of two neighbouring cells in a non-conforming mesh. The two right nodes from cell J, the two left nodes from cell K, and the two left nodes from cell L are involved in the computation of the flux in the boundary integral of Equation (4) for face e.

3 | NUMERICAL RESULTS

We consider a number of benchmarks of atmospheric flows over orography for the validation of NWP codes; for example, see the seminal papers of Klemp and Durran (1983); Klemp and Lilly (1978) and the results and discussions in Bonaventura (2000); Melvin *et al.* (2019); Pinty *et al.* (1995); Tumolo and Bonaventura (2015). The objective of these tests is twofold. First, we evaluate the stability and accuracy of numerical solutions obtained using non-conforming meshes compared with those obtained using uniform meshes. Second, we assess the computational cost carried by both set-ups and potential advantages at a given accuracy level.

Discrete parameter choices for the numerical simulations are associated with two Courant numbers; namely, the acoustic Courant number C, based on the speed of sound c, and the advective Courant number C_u, based on the magnitude of the local flow velocity u:

$$C = rc\frac{\Delta t}{\mathcal{H}}, \qquad C_u = ru\frac{\Delta t}{\mathcal{H}}. \tag{5}$$

Here, r is the polynomial degree used for the DG spatial discretization, $\mathcal{H}$ is the minimum cell diameter of the computational mesh, and Δt is the time step adopted for the time discretization. We consider polynomial degree $r = 4$, unless stated differently. Wall boundary conditions are employed for the bottom boundary, whereas non-reflecting boundary conditions are required by the top boundary and the lateral boundaries. For this purpose, we introduce the following Rayleigh damping profile (Melvin *et al.* 2019; Orlando *et al.* 2023):

$$\lambda = \begin{cases} 0, & \text{if } z < z_B, \\ \overline{\lambda}\sin^2\left[\frac{\pi}{2}\left(\frac{z-z_B}{z-z_T}\right)\right], & \text{if } z \geq z_B, \end{cases} \tag{6}$$

where z_B denotes the height at which the damping starts and z_T is the top height of the domain considered. Analogous definitions apply for the two lateral boundaries. The classical Gal-Chen height-based terrain-following coordinate (Gal-Chen and Somerville 1975) is used to obtain a terrain-following mesh in Cartesian coordinates.

A relevant diagnostic quantity to check that a correct orographic response is achieved is represented by the vertical flux of horizontal momentum (henceforth "momentum flux"), defined as (Smith 1979)

$$m(z) = \int_{-\infty}^{\infty} \overline{\rho}(z) u'(x,z) w'(x,z)\, dx. \tag{7}$$

Here, u' and w' denote the deviation from the background state of the horizontal and vertical velocity respectively. Table 1 reports the parameters employed for the different test cases.

3.1 | Linear hydrostatic flow over a hill

First, we consider a linear hydrostatic configuration e.g. Giraldo and Restelli (2008); Orlando *et al.* (2023). The bottom boundary is described by the function

$$h(x) = \frac{\mathrm{h_c}}{1 + \left(\frac{x-x_c}{a_c}\right)^2}, \tag{8}$$

the so-called "versiera of Agnesi", with h_c being the height of the hill and a_c being its half-width. We take $h_c = 1$ m, $x_c = 120$ km, and $a_c = 10$ km. The initial state of the atmosphere consists of a constant horizontal flow with $\overline{u} = 20\ \mathrm{m \cdot s^{-1}}$ and of an isothermal background profile with temperature $\overline{T} = 250$ K and Exner pressure

$$\overline{\Pi} = \exp\left(-\frac{g}{c_p \overline{T}} z\right), \tag{9}$$

with $c_p = R\gamma/(\gamma - 1)$ denoting the specific heat at constant pressure. In an isothermal configuration the Brunt–Väisälä frequency is given by $N = g/(c_p\overline{T})^{1/2}$. Hence, one can easily verify that

$$\frac{Na_c}{\overline{u}} \gg 1, \tag{10}$$

meaning that we are in a hydrostatic regime (Giraldo and Restelli 2008; Pinty *et al.* 1995). The computational mesh is composed by $N_{\mathrm{el}} = 1{,}116$ elements with four different refinement levels (Figure 2). The finest level corresponds to a resolution of 300 m along x and of 62.5 m along z, whereas the coarsest level corresponds to a resolution of 2,400 m along x and of 500 m along z. From the linear theory, the analytical momentum flux is given by Smith (1979)

$$m^H = -\frac{\pi}{4}\overline{\rho}_s \overline{u}_s N h_c^2, \tag{11}$$

with $\overline{\rho}_s$ and $\overline{u}_s$ denoting the surface background density and velocity respectively. The computed momentum flux

TABLE 1 Model parameters for the two-dimensional test cases in Section 3; see main text for details.

Test case	Δt (s)	T_f (hr)	Domain (km × km)	Damping layer x	Damping layer z	$\overline{\lambda}\Delta t$	C	C_u
LHMW	2.5	15	240 × 30	(0, 80), (160,240)	(15, 30)	0.3	3.66	0.23
NLNHMW	1	5	40 × 20	(0, 10), (30, 40)	(9, 20)	0.15	2.16	0.13
BWS	0.75	3	220 × 25	(0, 30), (190,220)	(20, 25)	0.15	0.79	0.23
T-REX	0.75	4	400 × 26	(0, 50), (350,400)	(20, 26)	0.15	1.34	0.29

Note: The intervals where the damping layers are applied are in units of kilometres.
Abbreviations: BWS, Boulder windstorm (inviscid configuration); LHMW, linear hydrostatic mountain wave; NLNHMW, nonlinear non-hydrostatic mountain wave; T-REX, Terrain-Induced Rotor Experiment, Sierra profile.

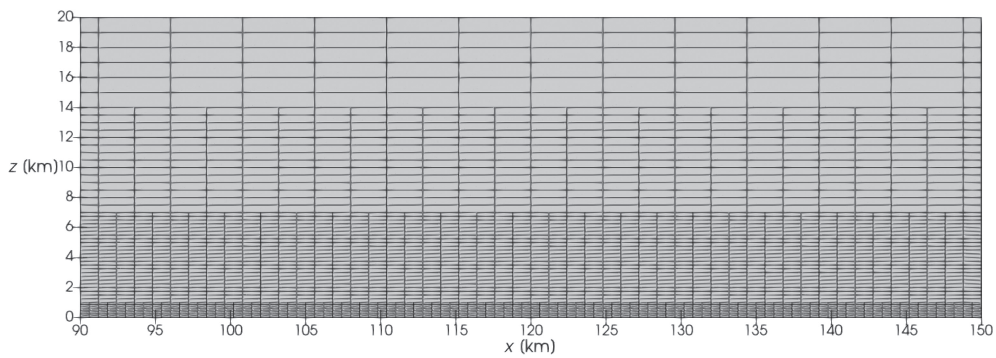

FIGURE 2 Linear hydrostatic flow over a hill; non-conforming mesh.

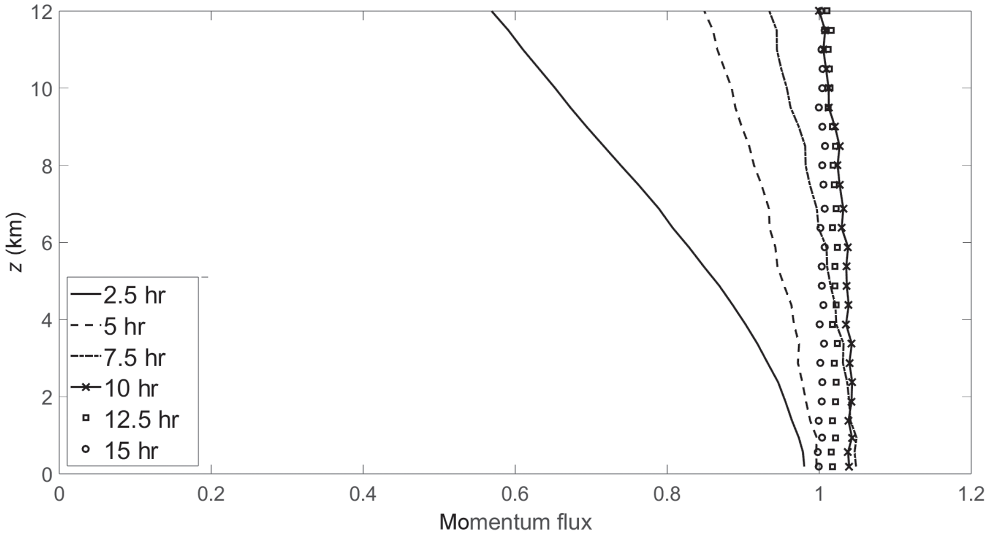

FIGURE 3 Linear hydrostatic flow over a hill; evolution of normalized momentum flux for the simulation using a non-conforming mesh.

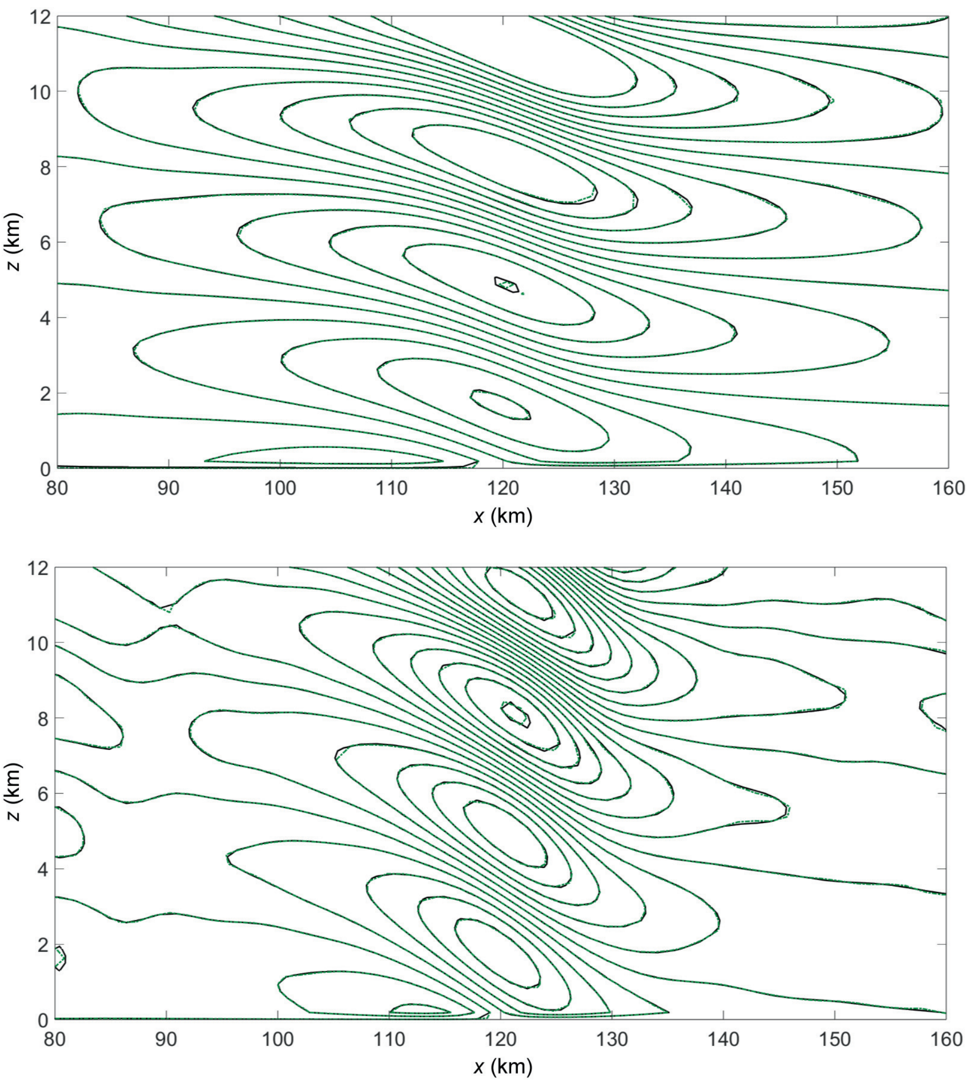

FIGURE 4 Linear hydrostatic flow over a hill at $t = T_f = 15$ hr; numerical solutions using a non-conforming mesh (solid lines) and the finest uniform mesh (dashed dotted lines). Top: horizontal velocity deviation; contours in $[-2.5, 2.5] \times 10^{-2}$ m·s^{-1} with a 5×10^{-3} m·s^{-1} contour interval. Bottom: vertical velocity; contours in $[-4, 4] \times 10^{-2}$ m·s^{-1} with a 5×10^{-4} m·s^{-1} contour interval.

normalized by m^H approaches 1 as the simulation reaches the steady state (Figure 3). The momentum is correctly transferred in the vertical direction, and no spurious oscillations arise at the interface between different mesh levels.

A reference solution is computed using a uniform mesh with the maximum resolution of the non-conforming mesh, namely a mesh composed by 200 elements along the horizontal direction and 120 elements

TABLE 2 Linear hydrostatic flow over a hill: horizontal resolution Δx, vertical resolution Δz, l^2 relative errors on the momentum flux, and wall-clock times (WT) for the uniform meshes and the non-conforming meshes.

	Uniform				Non-conforming				
N_{el}	Δx (m)	Δz (m)	$m(z)$ error	WT (s)	Δx_{min} (m)	Δz_{min} (m)	$m(z)$ error	WT (s)	Speed-up
402	895.52	1250	6.10×10^{-2}	3050	1200	250	4.34×10^{-3}	4210	
504	952.38	937.5	1.96×10^{-2}	3180	600	125	2.34×10^{-3}	6510	
1,116	967.74	416.67	3.94×10^{-3}	4470	300	62.5	2.53×10^{-3}	14800	8.9
24,000	300	62.5	—	131600	—	—	—	—	

Note: The speed-up is computed considering the same maximum spatial resolution; that is, comparing the WT of the finest uniform mesh and the WT of the coarsest non-conforming mesh (bold WT; also see main text for further details).
Abbreviation: N_{el}, number of elements.

along the vertical one. A comparison of contour plots for the horizontal velocity deviation and for the vertical velocity shows an excellent agreement in the lee waves simulation between the finest uniform mesh and the non-conforming mesh (Figure 4).

In order to further emphasize the results obtained with the use of the non-conforming mesh, we consider a uniform mesh with the same number of elements ($62 \times 18 = 1{,}116$) of the non-conforming mesh. From a quantitative point of view, we compute relative errors with respect to the reference solution in the portion of the domain $\Omega = [80{,}160]$ km $\times$ $[0, 12]$ km (Table 2). Moreover, we consider different configurations with non-conforming meshes and we compare them with configurations employing a uniform mesh using the same number of elements. Non-conforming mesh simulations significantly outperform uniform mesh simulations in terms of accuracy at a given number of degrees of freedom. At the finest 300 m horizontal resolution and 62.5 m vertical resolution, the use of the non-conforming mesh leads to a computational time saving of around 90% over the corresponding uniform mesh (bold numbers in Table 2). However, the present non-conforming mesh implementation is instead less competitive considering the wall-clock time at a given number of elements. This is due to the fact that, on non-conforming meshes, the condition number of the linear systems resulting from the IMEX discretization increases substantially, leading to a higher number of iterations for the generalized minimal residual solver (Du *et al.* 2009; Kamenski *et al.* 2014; Orlando *et al.* 2022). Although some effective geometric multigrid preconditioners are available for non-symmetric systems arising from elliptic equations (Bramble *et al.* 1994; Esmaily *et al.* 2018), their extension to hyperbolic problems and their implementation in the context of the matrix-free approach of the deal.II library is not straightforward and will be the subject of future work.

3.2 | Nonlinear non-hydrostatic flow over a hill

Next, we consider a non-hydrostatic regime for which

$$\frac{Na_c}{\overline{u}} \approx 1. \tag{12}$$

More specifically, we focus on a nonlinear non-hydrostatic case (Orlando *et al.* 2023; Restelli 2007; Tumolo and Bonaventura 2015). The bottom boundary is described again by Equation (8), with $h_c = 450$ m, $x_c = 20$ km, and $a_c = 1$ km. The initial state of the atmosphere is described by a constant horizontal flow with $\overline{u} = 13.28\ \text{m}\cdot\text{s}^{-1}$ and by the following potential temperature and Exner pressure:

$$\overline{\theta} = \theta_{\text{ref}} \exp\left(\frac{N^2}{g} z\right), \tag{13}$$

$$\overline{\Pi} = 1 + \frac{g^2}{c_p \theta_{\text{ref}} N^2}\left[\exp\left(-\frac{N^2}{g} z\right) - 1\right], \tag{14}$$

with $\theta_{\text{ref}} = 273$ K and $N = 0.02\ \text{s}^{-1}$. The mesh is composed by $N_{el} = 282$ elements with three different resolution levels (Figure 5). The finest level corresponds to a resolution of 208.33 m along x and of 104.17 m along z, whereas the coarsest level corresponds to a resolution of around 833.33 m along x and of 416.67 m along z.

A reference solution is computed using a uniform mesh with $48 \times 48 = 2{,}304$ elements, which corresponds to the finest resolution of the non-conforming mesh. A comparison of contour plots for the horizontal velocity deviation and for the vertical velocity shows good agreement between the finest uniform mesh and the non-conforming mesh in the development of lee waves (Figure 6). The use of the non-conforming mesh yields a computational time saving of around 60% (bold numbers

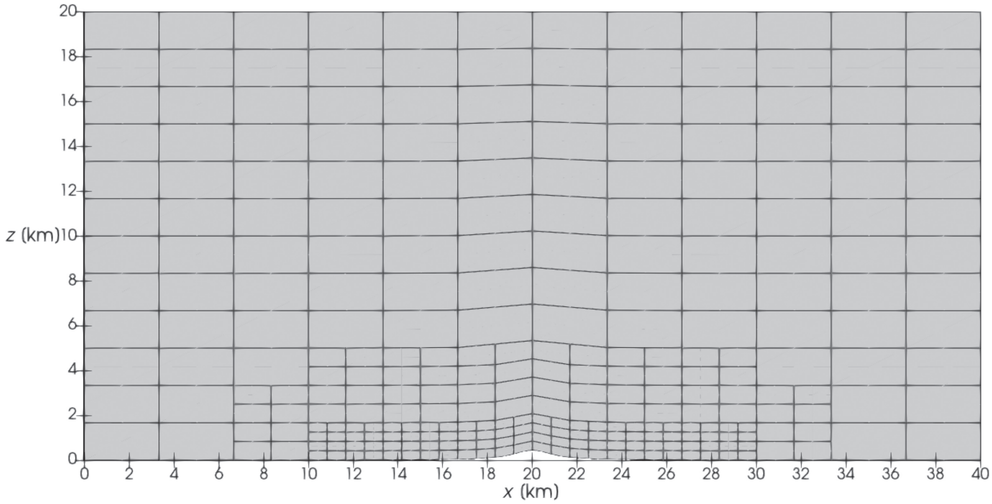

FIGURE 5 Nonlinear non-hydrostatic flow over a hill; non-conforming mesh.

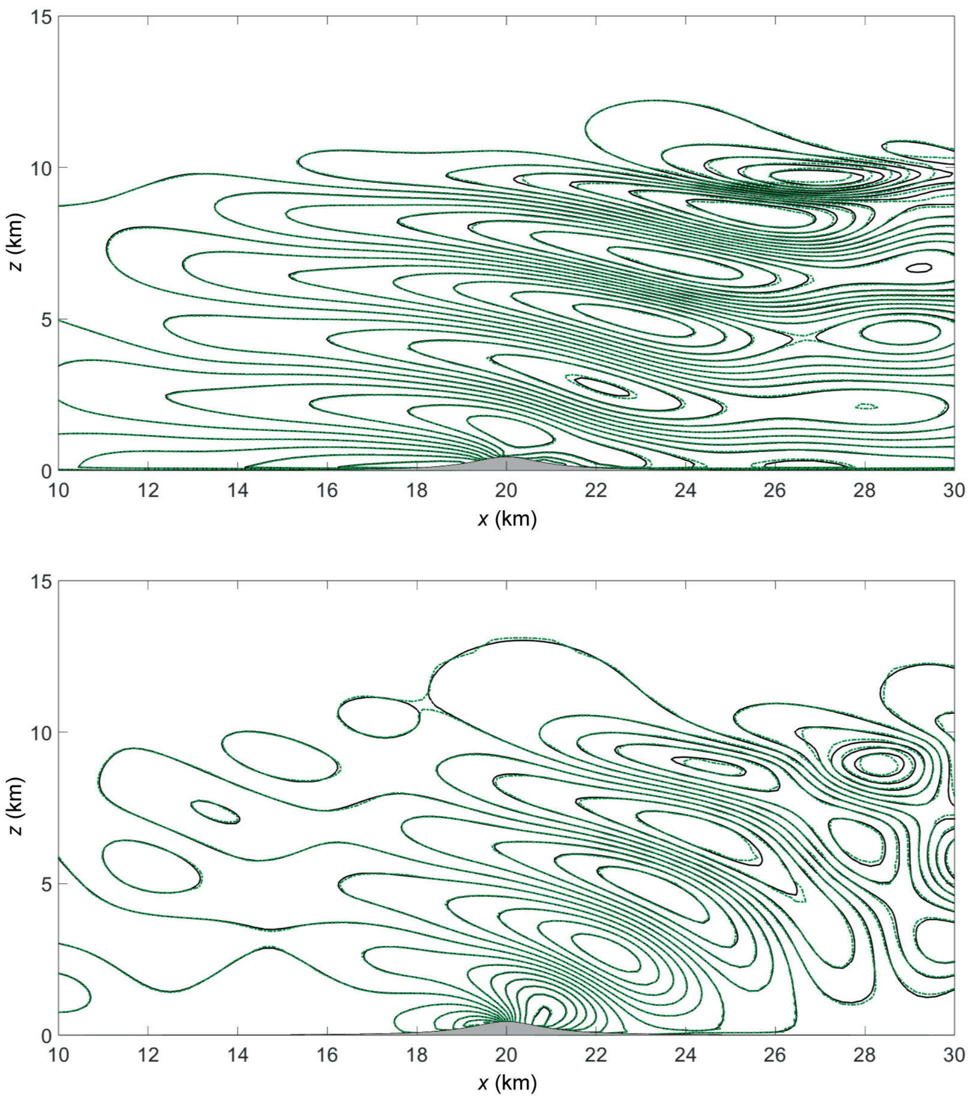

FIGURE 6 Nonlinear non-hydrostatic flow over a hill at $t = T_f = 5$ hr, computed on the finest uniform mesh (solid lines) and on a non-conforming mesh (dashed -dotted lines). Top: horizontal velocity deviation; contours in the interval $[-7.2, 9.0]$ m·s^{-1} with a 1.16 m·s^{-1} interval. Bottom: vertical velocity; contours in the interval $[-4.2, 4.0]$ m·s^{-1} with a 0.586 m·s^{-1} interval.

in Table 3). In addition, we consider a mesh with uniform resolution and with the same number of elements $47 \times 6 = 282$ of the non-conforming mesh. We compare the computed normalized momentum flux at $t = T_f$ in the reference configuration, in the non-conforming mesh configuration, and in the configuration with a uniform

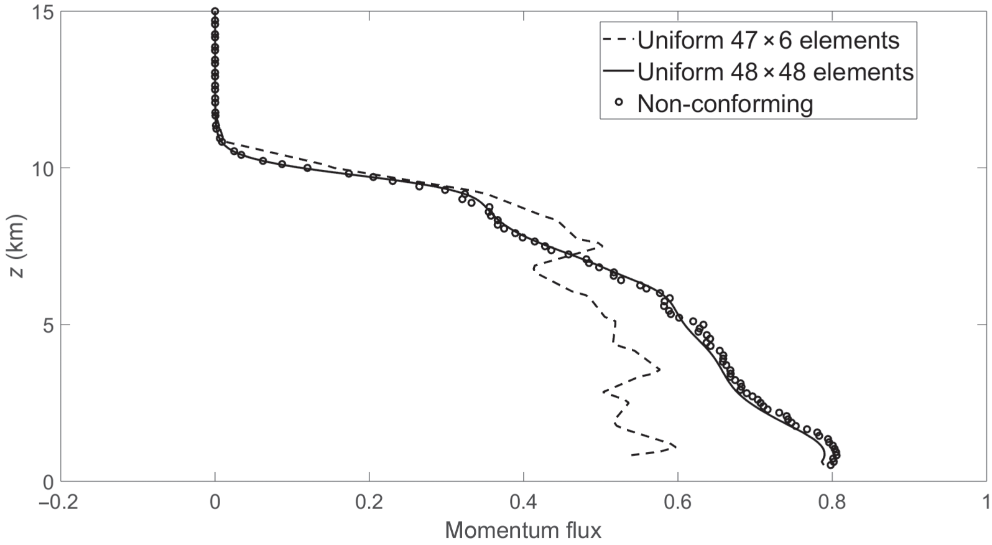

FIGURE 7 Nonlinear non-hydrostatic flow over a hill; comparison of normalized momentum flux at $t = T_f = 5$ hr obtained using a uniform mesh at fine resolution (solid line), a uniform mesh with the same number of elements of the non-conforming mesh (dashed line), and the non-conforming mesh (dots).

TABLE 3 Nonlinear non-hydrostatic flow over a hill: horizontal resolution Δx, vertical resolution Δz, l^2 relative errors on the momentum flux, and wall-clock times (WT) for the uniform meshes and the non-conforming mesh.

N_{el}	Δx (m)	Δz (m)	$m(z)$ error	WT (s)	Speed-up
282 (uniform)	212.77	833.33	2.31×10^{-1}	4520	
282 (non-conforming)	208.33	104.17	1.92×10^{-2}	9680	2.3
2304 (uniform)	208.33	104.17	—	22500	

Note: The speed-up is computed comparing the WT of the finest uniform mesh and the WT of the non-conforming mesh, which have the same resolution (bold WT; also see main text for further details).
Abbreviation: N_{el}, number of elements.

mesh with the same number of elements of the non-conforming mesh (Figure 7). In terms of relative error with respect to the reference solution, the locally refined non-conforming mesh outperforms the uniform mesh by about an order of magnitude using the same number of elements (Table 3). Analogous considerations to those reported in Section 3.1 are valid for the computational time.

3.3 | January 11, 1972, Boulder windstorm

Next, we consider the more realistic condition of the January 11, 1972, Boulder (Colorado) windstorm benchmark (Doyle *et al.* 2000). This test case is particularly challenging because a complex wave-breaking response is established aloft in the lee of the mountain. The initial conditions are horizontally homogeneous and based upon the upstream measurements at 1200 UTC, January 11, 1972, Grand Junction, Colorado, as shown in Doyle *et al.* (2000). The initial conditions contain a critical level near $z =$ 21 km (Figure 8), which more realistically simulates the stratospheric gravity-wave breaking (Doyle *et al.* 2000). The pressure is computed from the hydrostatic balance; namely:

$$p(z) = p_0 \exp\left(-\frac{g}{R}\int_0^z \frac{1}{T(s)}\, ds\right), \qquad (15)$$

with $p_0 = 10^5$ Pa. Linear interpolation is employed to evaluate both temperature and horizontal velocity.

The bottom boundary is described by Equation (8), with $h_c = 2$ km, $x_c = 100$ km, and $a_c = 10$ km. We consider two different computational meshes: a uniform mesh composed of $120 \times 60 = 7{,}200$ elements (i.e., a resolution of 458.33 m along the horizontal direction and of 104.17 m along the vertical one), and a non-conforming mesh with three different levels, composed of $N_{el} = 1{,}524$, with the finest level corresponding to the resolution of the uniform mesh.

The horizontal velocity and the potential temperature computed at $t = T_f$ by the IMEX-DG method using a uniform mesh are in reasonable agreement with the reference results (Doyle *et al.* 2000), in particular for what concerns the potential temperature (Figure 9). Numerous regions

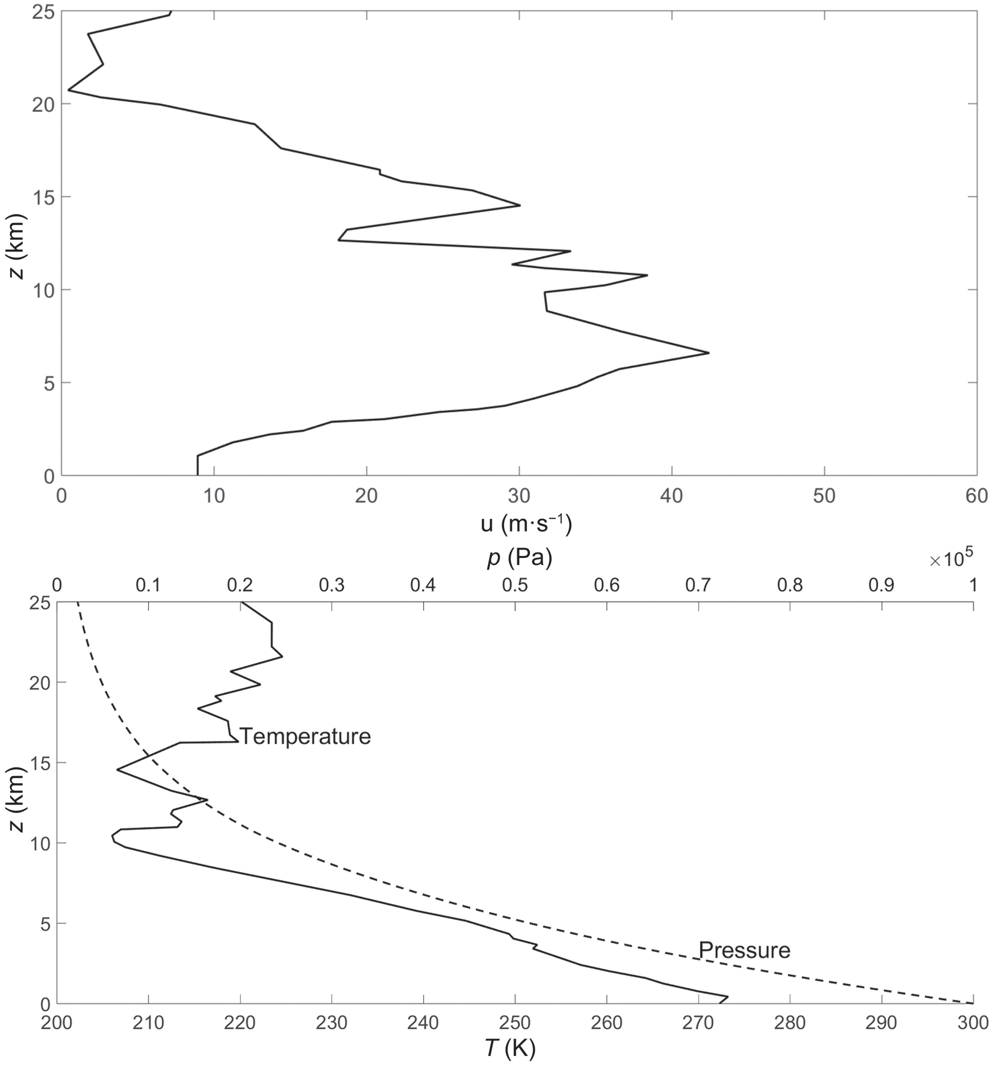

FIGURE 8 Boulder windstorm test case, initial conditions. Top: horizontal velocity. Bottom: temperature (solid line) and pressure (dashed line)

of small-scale motion and larger high-frequency spatial structures arise with respect to the other tests using the uniform mesh, because of the lack of a subgrid eddy viscosity. The qualitative behaviour of the simulation with the uniform mesh and the one with the non-conforming mesh is in good agreement, even though visible differences arise in the deep regions of wave breaking in the stratosphere (Figure 9). In terms of wall-clock time, the configuration with the non-conforming mesh is about 65% computationally cheaper than the configuration with the uniform mesh (3.75×10^4 s vs. 1.37×10^4 s).

Following Doyle *et al.* (2011), we then compute the momentum flux, Equation (7), using the mean value of u and w to compute u' and w'. A comparison at final time of the vertical flux of horizontal momentum, Equation (7), normalized by its values at the surface obtained with the uniform mesh displays a reasonable agreement between the two simulations, especially for z above 12 km (Figure 10). The discrepancy in the vertical region between $z = 7$ km and $z = 12$ km is probably due to the development of small-scale features and to the lack of subgrid eddy viscosity parametrization, as already discussed for the contour plots.

Next, we repeat the simulations for this test case including a simplified model for turbulent vertical diffusion for NWP applications, originally proposed in Louis (1979) and also discussed in Benard *et al.* (2000); Bonaventura and Ferretti (2014); Girard and Delage (1990). As commonly done in numerical models for atmospheric physics, we resort to an operator splitting approach. The diffusion model is treated with the implicit part of the IMEX method, which corresponds to the TR-BDF2 scheme (Hosea and Shampine 1996; Orlando *et al.* 2022). The nonlinear diffusivity κ has the form

$$\kappa\left(\frac{\partial u}{\partial z}, \frac{\partial \theta}{\partial z}\right) = l^2 \left|\frac{\partial u}{\partial z}\right| F(\mathrm{Ri}). \qquad (16)$$

Here, l is a mixing length and Ri is the Richardson number given by

$$\mathrm{Ri} = \frac{g}{\theta_0} \frac{\partial \theta / \partial z}{|\partial u / \partial z|^2}, \qquad (17)$$

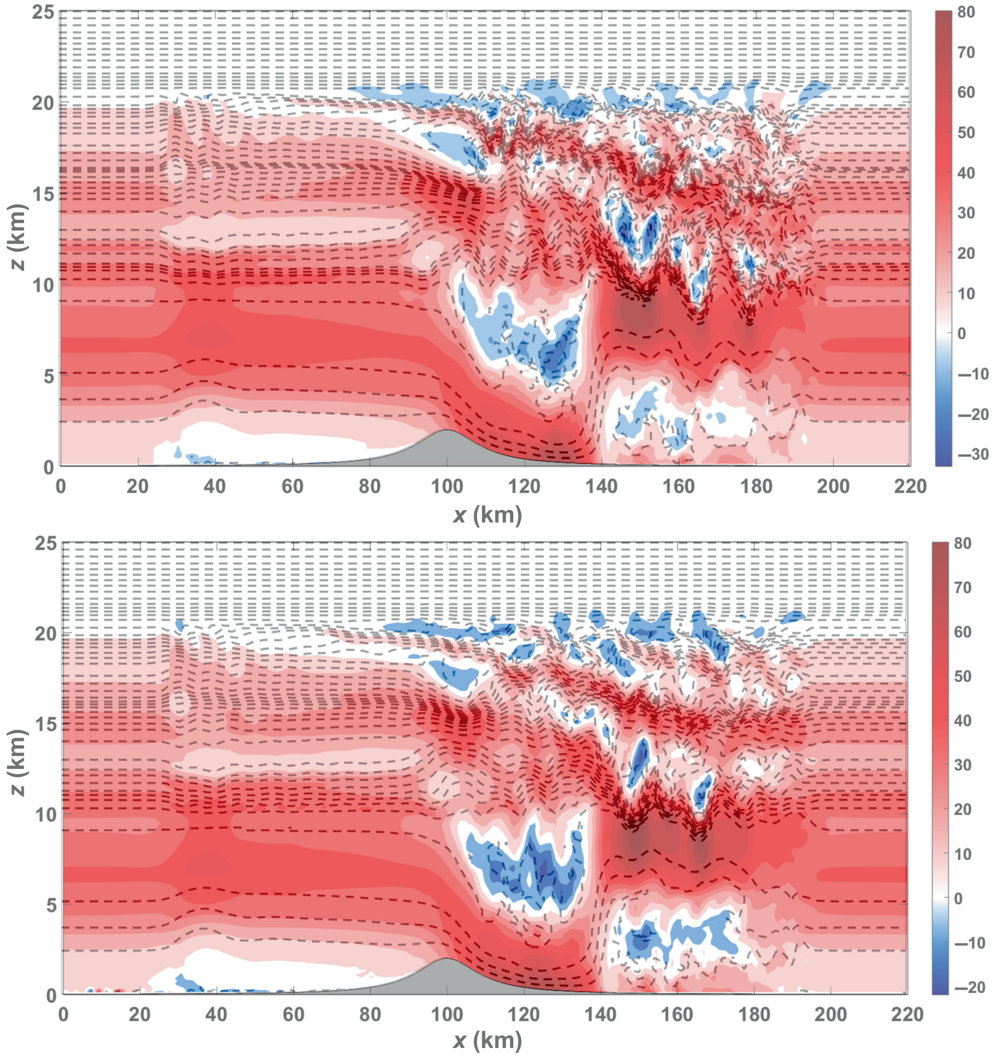

FIGURE 9 Boulder windstorm test case numerical results at $t = T_f = 3$ hr. Top: uniform mesh. Bottom: non-conforming mesh. Horizontal velocity (colours), contours in the range $[-40, 80]\ \mathrm{m \cdot s^{-1}}$ with a $8\ \mathrm{m \cdot s^{-1}}$ interval. Potential temperature (dashed lines), contours in the range $[273, 650]$ K with an 8 K interval.

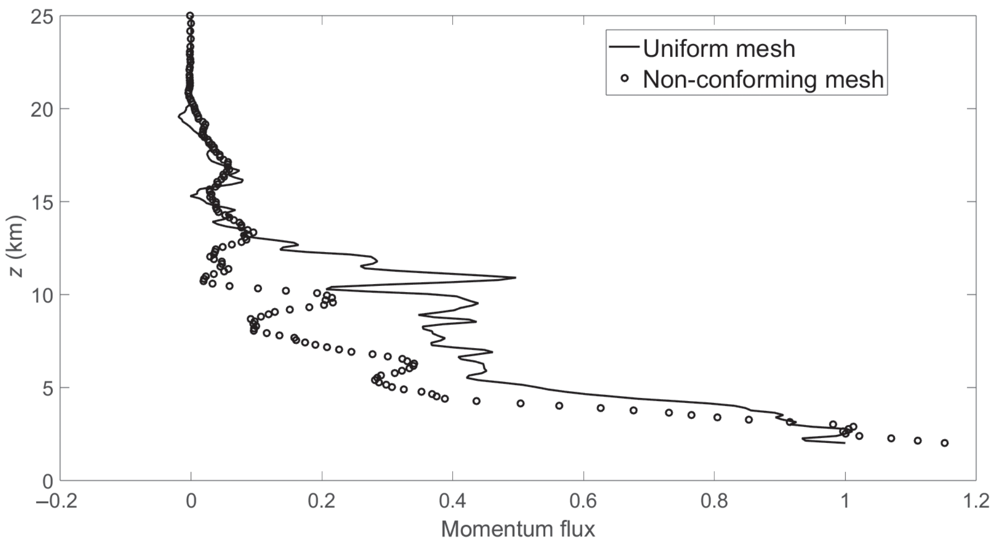

FIGURE 10 Boulder windstorm test case; comparison of normalized momentum flux at $t = T_f = 3$ hr computed using the uniform mesh (solid line) and the non-conforming mesh (dots).

with θ_0 denoting a reference temperature. Finally, the function $F(\mathrm{Ri})$ is defined as

$$F(\mathrm{Ri}) = (1 + b|\mathrm{Ri}|)^{\beta}, \tag{18}$$

where

$$\begin{cases} \beta = -2, b = 5 & \text{if } \mathrm{Ri} > 0, \\ \beta = \frac{1}{2}, b = 20 & \text{if } \mathrm{Ri} < 0. \end{cases} \tag{19}$$

Quarterly Journal of the Royal Meteorological Society RMetS

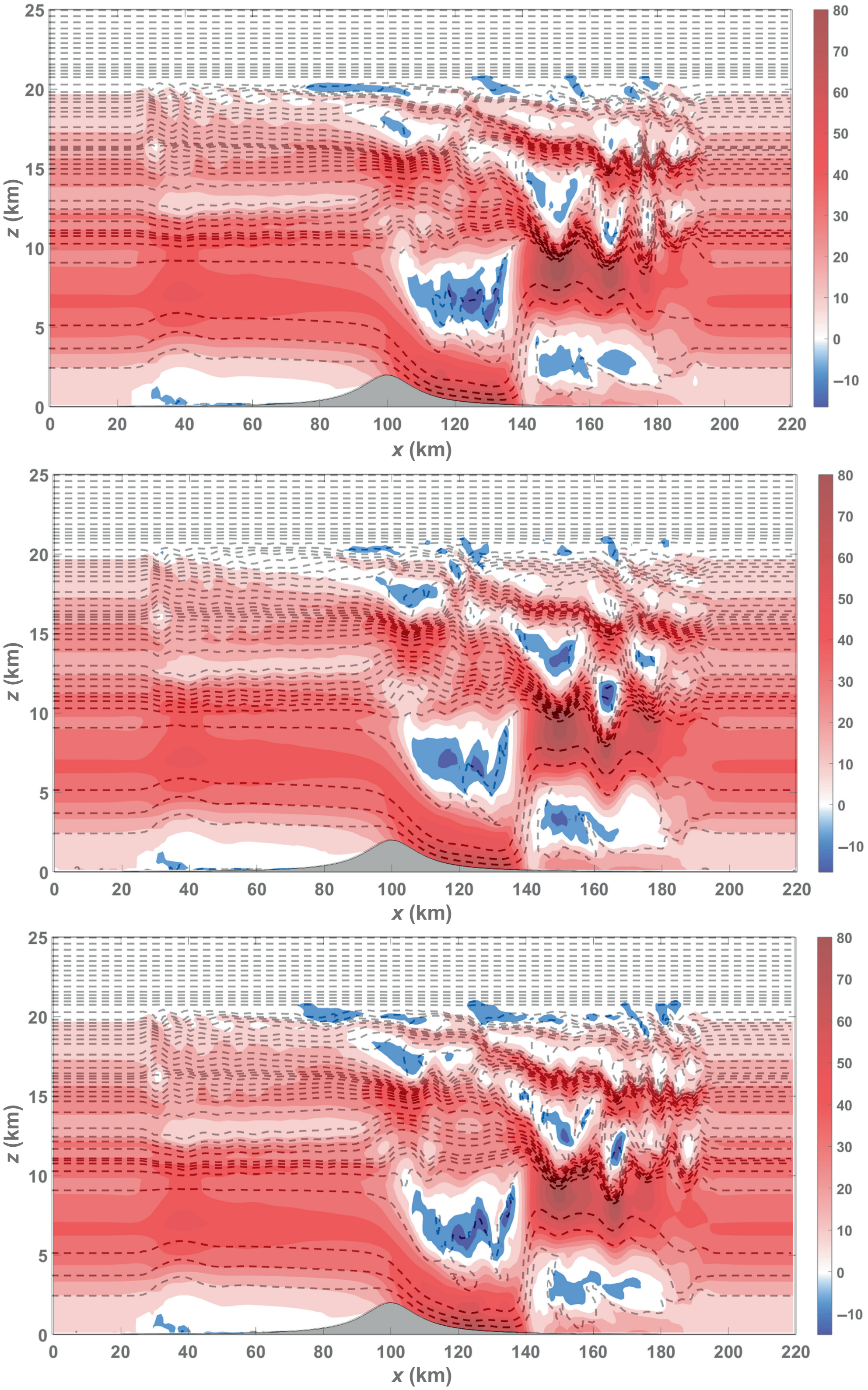

FIGURE 11 Boulder windstorm test case with turbulent vertical diffusion. Top: uniform mesh. Middle: coarse non-conforming mesh. Bottom: fine non-conforming mesh. Horizontal velocity (colours), contours in the range $[-40, 80]\,\mathrm{m\cdot s^{-1}}$ with an $8\,\mathrm{m\cdot s^{-1}}$ interval. Potential temperature (dashed lines), contours in the range [273,650] K with an 8 K interval.

We consider the uniform mesh with $120 \times 60 = 7{,}200$ elements and a coarse non-conforming mesh with $N_{\mathrm{el}} = 1{,}524$ elements already employed for the inviscid case. In addition, we consider a fine non-conforming mesh with three different refinement levels and $N_{\mathrm{el}} = 6{,}324$ elements. The fine resolution around the orography is of 229.17 m along the horizontal direction and of 52.08 m along the vertical one. We use a time step $\Delta t = 0.375$ s, corresponding to a maximum acoustic Courant number $C \approx 0.79$ and a maximum advective Courant number

$C_u \approx 0.23$. Finally, we take $l = 100$ m and $\theta_0 = 273$ K in Equation (16).

At $t = T_f$, numerical solutions computed using the uniform mesh and the non-conforming mesh are in good agreement for both the horizontal velocity and the potential temperature, in particular for the finest non-conforming mesh (Figure 11). In terms of wall-clock time, a computational time saving of around 50% is achieved with the coarse non-conforming mesh (bold numbers in Table 4), whereas performance is less optimal for the fine non-conforming mesh (see the discussion in Section 3.1). Finally, a comparison at $t = T_f$ of the computed momentum flux, Equation (7), normalized by its values at the surface obtained with the uniform mesh suggests that the results of the uniform mesh are approached as long as the resolution of the non-conforming mesh increases (Figure 12).

3.4 | Terrain-Induced Rotor Experiment mountain wave

Next, we consider simulations of a flow over a steep real orography (Doyle *et al.* 2011; Kühnlein *et al.* 2013), as shown in Figure 13. The initial state is horizontally homogeneous and it is based on conditions during Intensive Observation Period 6 of the Terrain-Induced Rotor Experiment (Doyle *et al.* 2011), as reported in Figure 14. We consider a DG spatial discretization using degree $r = 2$ polynomials and three computational meshes: a uniform mesh composed of $400 \times 60 = 24{,}000$ elements, corresponding to a resolution of 500 m along the horizontal direction and of 216.66 m along the vertical direction, and two non-conforming meshes. The coarsest non-conforming mesh consists of three different levels and $N_{el} = 5{,}298$ elements, whereas the finest non-conforming mesh is obtained with a global refinement of the coarsest non-conforming mesh, with $N_{el} = 21{,}792$ elements (Figure 15). The finest level of the coarsest non-conforming mesh corresponds to the resolution of the uniform mesh. Hence, the fine resolution around the orography for the finest non-conforming mesh is 250 m along the horizontal direction and 108.33 m along the vertical direction. We take $l = 100$ m and $\theta_0 = 273$ K in Equation (16). The vertical turbulent diffusion model is necessary to obtain a stable numerical solution.

Both in the horizontal velocity and in the potential temperature variables, the IMEX-DG numerical solutions

TABLE 4 Boulder windstorm test case with turbulent vertical diffusion: horizontal resolution Δx, vertical resolution Δz, and wall-clock times (WT) for the uniform mesh and the non-conforming meshes.

N_{el}	Δx (m)	Δz (m)	WT (s)	Speed-up
7200 (uniform)	458.33	104.17	119,000	
1524 (non-conforming)	458.33	104.17	51,900	2.3
6324 (non-conforming)	229.17	52.08	160,000	

Note: The speed-up is computed considering the same maximum spatial resolution; that is, comparing the WT of the finest uniform mesh and the WT of the non-conforming mesh (bold WT; also see main text for further details).
Abbreviation: N_{el}, number of elements.

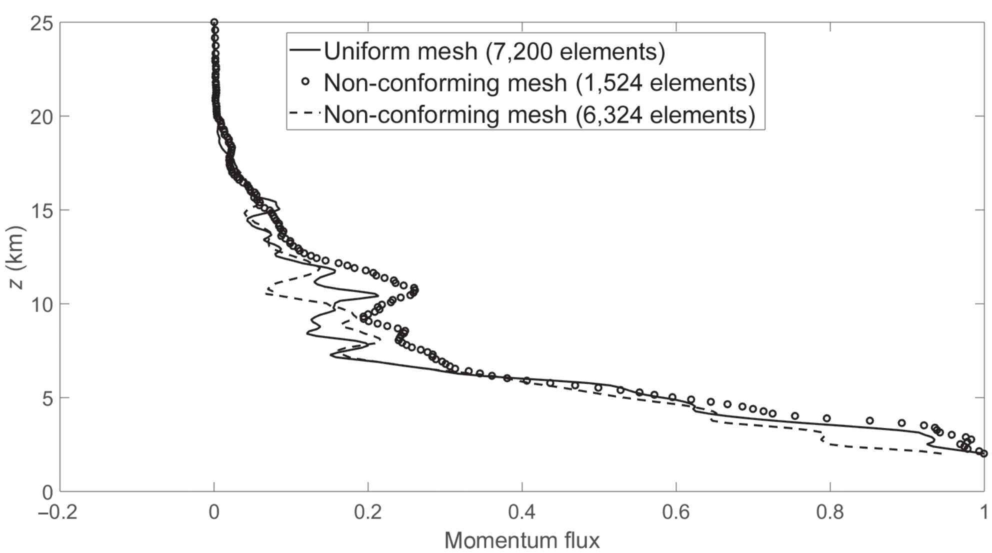

FIGURE 12 Boulder windstorm test case; comparison of normalized momentum flux at $t = T_f = 3$ hr between the uniform mesh (solid line), the fine (dashed line), and the coarse (dots) non-conforming meshes.

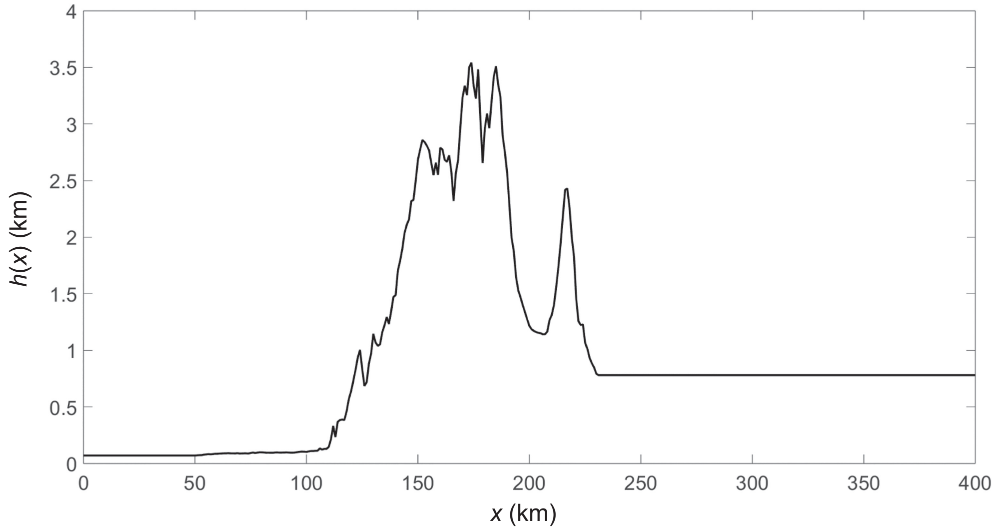

FIGURE 13 Terrain-Induced Rotor Experiment mountain-wave test, Sierra profile.

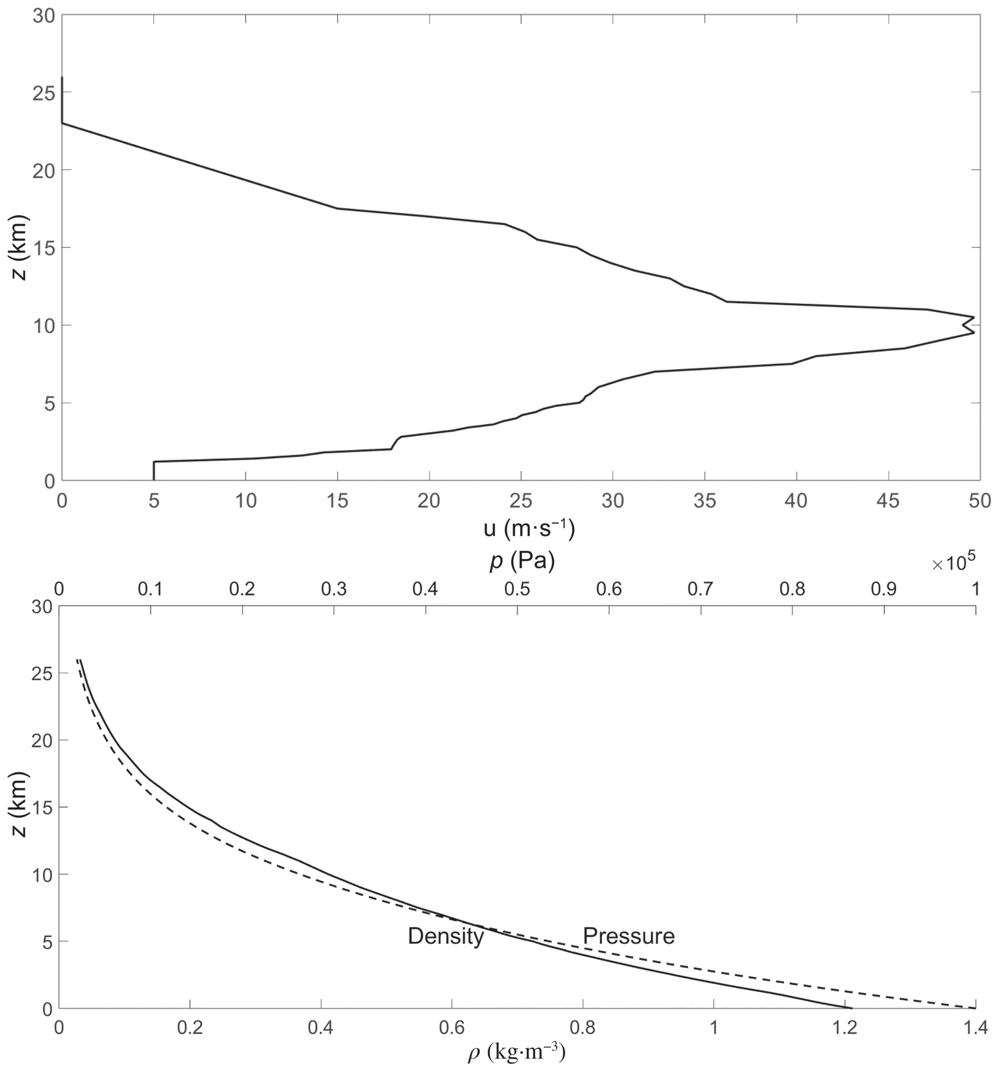

FIGURE 14 Terrain-Induced Rotor Experiment mountain-wave test case, initial conditions. Top: horizontal velocity. Bottom: density (solid line) and pressure (solid line).

at $t = T_{\mathrm{f}}$ display reasonable agreement between results obtained using the uniform mesh and the non-conforming meshes, showing the robustness of the proposed approach based on non-conforming meshes also in the case of a realistic, steep orography (Figure 16). Some differences arise in the structures of the horizontal velocity, but, unlike the

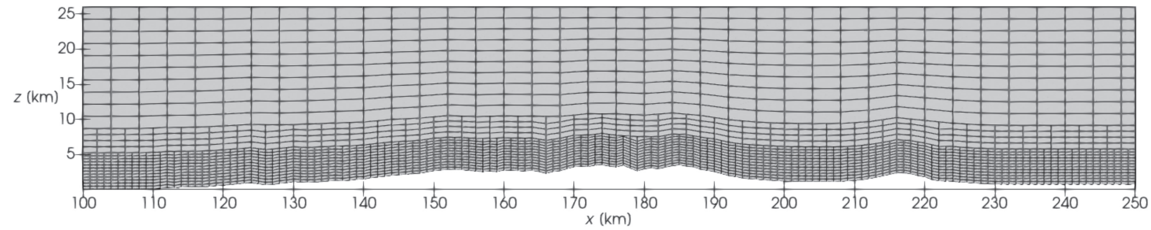

FIGURE 15 Terrain-Induced Rotor Experiment mountain wave, non-conforming mesh.

previous test case, in this benchmark (Doyle *et al.* 2011) there is low predictability of key characteristics such as the strength of downslope winds or the stratospheric wave breaking. Moreover, the change in the resolution of the topography has been shown to modify the representation of mountain-wave-driven middle-atmosphere processes (Kanehama *et al.* 2019). The contour plots show overall a reasonable agreement with those reported in Doyle *et al.* (2011). Although we have employed the same range values adopted in Doyle *et al.* (2011), one can easily notice that a lower minimum value of the velocity around $x \approx 220$ km and $z \approx 11$ km is achieved for the finest non-conforming mesh. This is likely due to the use of a high-order method with low numerical dissipation and to the increased resolution. For the sake of completeness, we have also run a simulation up to $t = 5$ hr and no numerical instability arises.

A far-field comparison of the momentum flux, Equation (7), confirms the low predictability of large-scale orographic features for this test case (Figure 17). On the other hand, one can easily notice that the momentum flux profiles shown in Figure 17 yield values of the same order of magnitude as those obtained with the models compared in Doyle *et al.* (2011). More specifically, the BLASIUS model employed in Doyle *et al.* (2011) predicts the lowest values, whereas the ASAM model predicts the highest ones. The values obtained in our framework, especially those established with the finest non-conforming mesh, are close to the mean values of all the models compared in Doyle *et al.* (2011). Similar to Section 3.3, a computational time saving of around 25% is achieved with the coarse non-conforming mesh (bold numbers in Table 5), whereas performance is less optimal for the fine non-conforming mesh.

3.5 | A 3D medium-steep bell-shaped hill

Finally, we consider a 3D configuration focusing on the flow over a bell-shaped hill discussed, for example, in Melvin *et al.* (2019); Orlando *et al.* (2023), which we briefly recall here for the convenience of the reader. The computational domain is $\Omega = (0, 60) \times (0, 40) \times (0, 16)$ km. The mountain profile is a 3D extension of the "versiera of Agnesi" and can be defined as

$$h(x, y) = \frac{h_c}{\left[1 + \left(\frac{x - x_c}{a_c}\right)^2 + \left(\frac{y - y_c}{a_c}\right)^2\right]^{3/2}}, \tag{20}$$

with $h_c = 400$ m, $a_c = 1$ km, $x_c = 30$ km, and $y_c = 20$ km. The buoyancy frequency is $N = 0.01\ \mathrm{s}^{-1}$, whereas the background velocity is $\overline{u} = 10\ \mathrm{m{\cdot}s^{-1}}$. Hence, since $Na_c/\overline{u} = 1$, we are in a non-hydrostatic regime. The background potential temperature and Exner pressure profiles are those reported in Section 3.2 with $\theta_{\mathrm{ref}} = 293.15$ K. The final time is $T_{\mathrm{f}} = 10$ hr. The damping layer is applied in the topmost 6 km of the domain and in the first and last 20 km along the lateral boundaries with $\overline{\lambda}\Delta t = 1.2$. We take polynomial degree $r = 4$ and we consider three different computational meshes: a coarse uniform mesh composed by $30 \times 20 \times 8 = 4{,}800$ elements (i.e., a resolution of 500 m along all the directions), a fine uniform mesh composed by $60 \times 40 \times 16$ elements (i.e. a resolution of 250 m), and a non-conforming mesh with three different levels, composed of $N_{\mathrm{el}} = 1{,}958$, with the finest level corresponding to the resolution of the finest uniform mesh (Figure 18). The time step is $\Delta t = 2$ s, yielding a maximum acoustic Courant number $C \approx 2.75$ and a maximum advective Courant number $C_u \approx 0.13$ for the finest uniform mesh. The contour plots of the vertical velocity on an x–y slice placed at $z = 800$ m and on an x–z slice placed at $y = 20$ km show once more the accuracy and the robustness of simulations employing non-conforming meshes (Figure 19). No spurious wave reflections arise at the internal boundaries that separate regions with different resolutions. Moreover, one can easily notice that the change of resolution affects the development of lee waves. However, it is sufficient to employ a higher resolution only around the orography, whereas larger scales along all the directions can be resolved at a much coarser resolution. The use of a non-conforming mesh yields a computational time saving of around 15% with respect to the coarse uniform mesh and of around 93% with respect to the fine uniform mesh (Table 6).

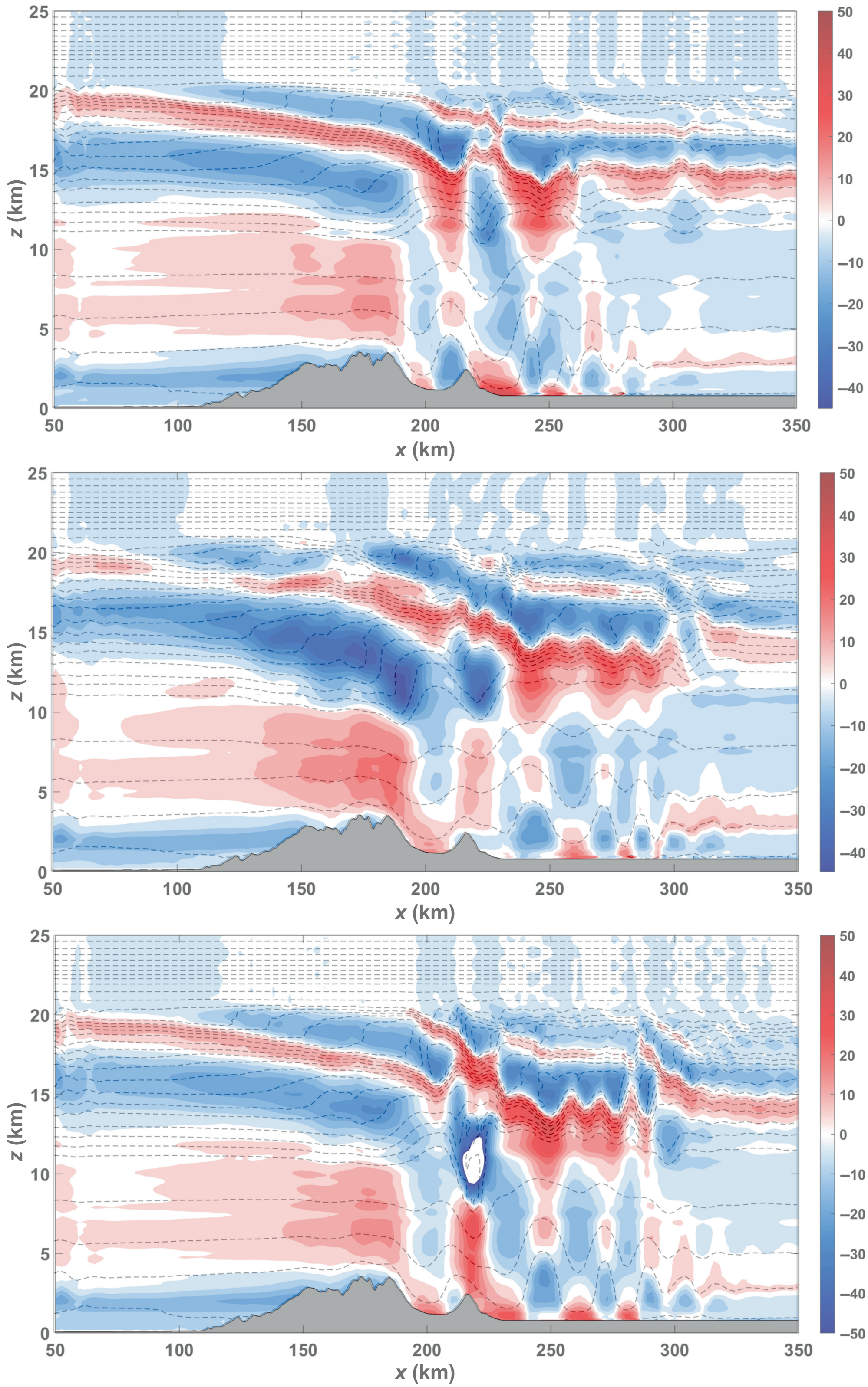

FIGURE 16 Terrain-Induced Rotor Experiment mountain-wave test case at $T_\mathrm{f} = 4\,\mathrm{hr}$. Top: uniform mesh. Middle: coarsest non-conforming mesh. Bottom: finest non-conforming mesh. Horizontal velocity perturbation (colours), contours in the range$[-50, 50]\,\mathrm{m{\cdot}s^{-1}}$ with a $2.5\,\mathrm{m{\cdot}s^{-1}}$ interval. Potential temperature (dashed lines), contours in the range $[273,650]\,\mathrm{K}$ with a $10\,\mathrm{K}$ interval.

4 | CONCLUSIONS

We have presented a systematic assessment of non-conforming meshes for the simulation of flows over orography using an IMEX-DG numerical model for the compressible Euler equations. For this purpose, we have exploited the adaptation framework provided by the open-source numerical library deal.II (Arndt *et al.* 2023; Bangerth *et al.* 2007). The proposed approach allows local mesh refinement both in the horizontal and vertical

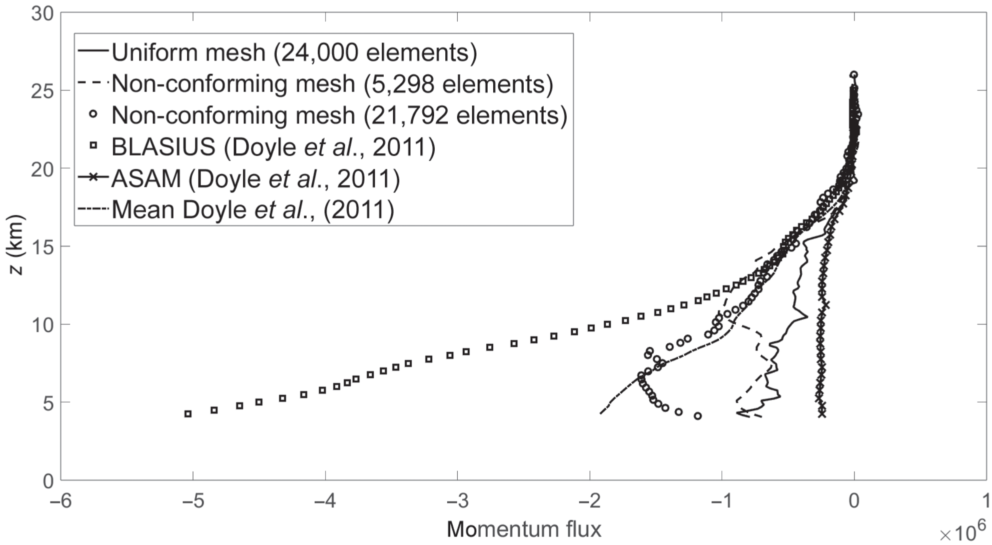

FIGURE 17 Terrain-Induced Rotor Experiment mountain-wave test case, comparison of momentum flux at $t = T_f = 4$ hr between the uniform mesh (solid line), the finest non-conforming mesh (dashed line), and the coarsest non-conforming mesh (dots). Results obtained in Doyle *et al.* (2011) are also reported. BLASIUS model (squares), ASAM model (crossed line), mean of all the models (dashed dotted line).

TABLE 5 Terrain-Induced Rotor Experiment mountain-wave test case: horizontal resolution Δx, vertical resolution Δz, and wall-clock times (WT) for the uniform mesh and the non-conforming meshes.

N_{el}	Δx (m)	Δz (m)	WT (s)	Speed-up
24,000 (uniform)	500	216.66	10,900	
5298 (non-conforming)	500	216.66	8390	1.3
21,792 (non-conforming)	250	108.33	16,500	

Note: The speed-up is computed considering the same maximum spatial resolution; that is, comparing the WT of the uniform mesh and the WT of the coarsest non-conforming mesh (bold WT; also see main text for further details).
Abbreviation: N_{el}, number of elements.

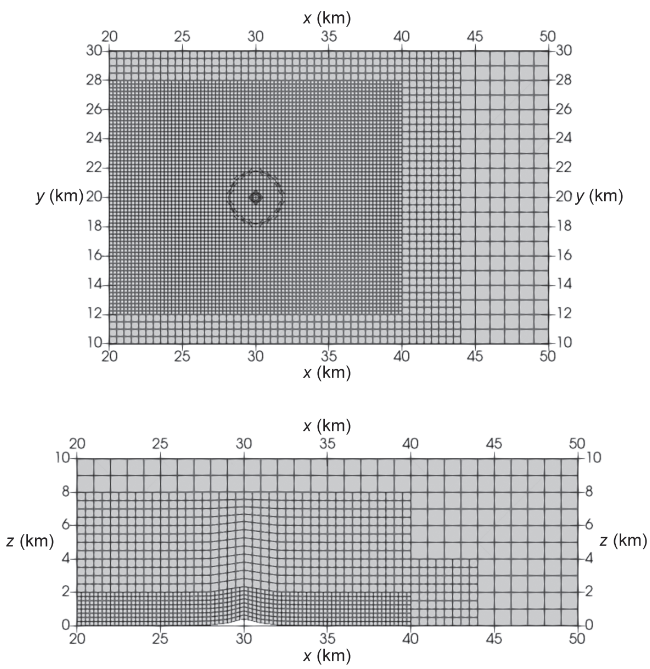

FIGURE 18 Three-dimensional medium-steep bell-shaped hill test case, non-conforming mesh. Left: x–y slice at $z = 800$ m. Right: x–z slice at $y = 20$ km.

directions without the need to apply relaxation procedures along the interfaces between the coarse and fine meshes. At a given accuracy level, the use of non-conforming meshes enables a significant reduction in the number of computational degrees of freedom with respect to uniform resolution meshes. The numerical results show that stable simulations are produced with no spurious reflections at internal boundaries separating mesh regions with different resolutions. In addition, accurate values for the momentum flux are retrieved in robust non-conforming simulations for increasingly realistic orography profiles.

Numerical simulations with non-conforming meshes can use substantially higher resolution only near the orographic features, correctly reproducing the larger scale, far-field orographic response, while using meshes that are relatively coarse over most of the domain. In a context of spatial resolutions approaching the hectometric scale in NWP models, these results support the use of locally refined, non-conforming meshes as a reliable and effective tool to greatly reduce the dependence of atmospheric models on orographic wave drag parametrizations. Indeed, the results obtained in our framework envisage the use of locally refined, non-conforming meshes

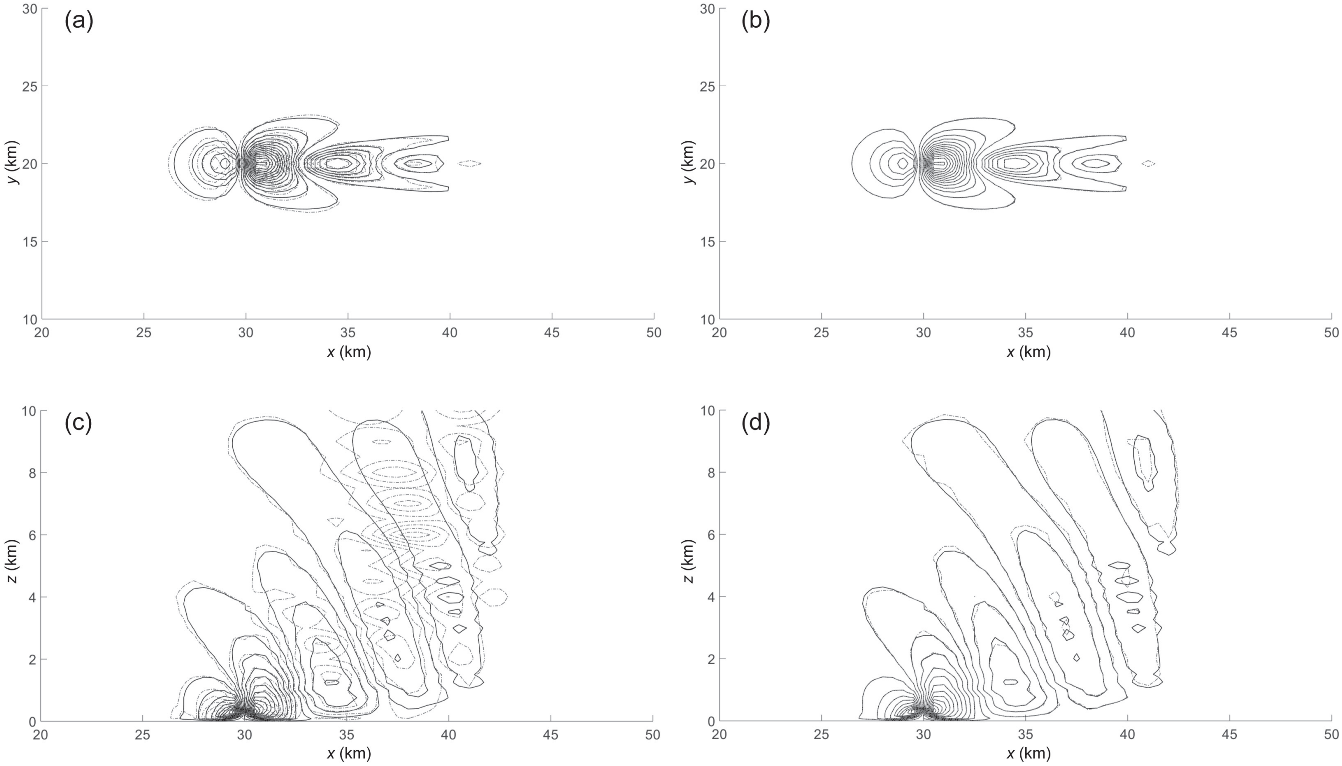

FIGURE 19 Three-dimensional medium-steep bell-shaped hill test case at $T_f = 10$ hr; vertical velocity contours. (a, c) Comparison between the fine uniform mesh (solid lines) and the coarse uniform mesh (dashed dotted lines) for x–y slice at $z = 800$ m in the range $[-1.5, 1.3]$ m·s^{-1} with a 0.1 m·s^{-1} interval. (c, d) Comparison between the fine uniform mesh (solid lines) and the non-conforming mesh (dashed dotted lines) for x–z slice at $y = 20$ km in the range $[-2.25, 2]$ m·s^{-1} with a 0.2 m·s^{-1} interval.

TABLE 6 Three-dimensional medium-steep bell-shaped hill test case: resolution Δ and wall-clock times (WT) for the uniform meshes and the non-conforming mesh.

N_{el}	Δ (m)	WT (s)	Speed-up
4800 (uniform)	500.0	3020	
38,400 (uniform)	250.0	36500	
1958 (non-conforming)	250.0	2560	14

Note: The speed-up is computed considering the same maximum spatial resolution; that is, comparing the WT of the finest uniform mesh and the WT of the non-conforming mesh (bold WT; also see main text for further details). Abbreviation: N_{el}, number of elements.

as a reliable, effective tool to push NWP and climate models out of the "grey zone" with respect to the resolution of orographic effects (Kanehama *et al.* 2019; Sandu *et al.* 2019).

In future developments, we will implement specific multilevel preconditioners in the matrix-free approach of the deal.II library in order to get the full benefit from the significant reduction in number of degrees of freedom allowed by the use of non-conforming meshes for more realistic configurations. We also plan to consider the inclusion of more complex physical phenomena, such as more sophisticated turbulence models, water vapour transport, and adiabatic heating, as well as exploring physics–dynamics coupling, in order to demonstrate that all the typical features of a high-resolution NWP model can be included in the proposed adaptive framework without loss of accuracy. Moreover, the proper thermodynamic description of atmosphere dynamics is becoming a matter of deep investigation (Staniforth 2022). The assumption of an ideal gas for dry air and water vapour (Staniforth and White 2019) is not always a proper one, especially if phase changes occur. Recent work by two of the authors (Orlando *et al.* 2022) can handle more general equations of state for real gases, thus paving the way to the inclusion of effects due to water vapour and moist species in a more realistic framework.

AUTHOR CONTRIBUTIONS

Giuseppe Orlando: conceptualization; investigation; methodology; resources; software; validation; visualization; writing – original draft; writing – review and editing. **Tommaso Benacchio:** conceptualization; investigation; supervision; visualization; writing – review and editing. **Luca Bonaventura:** conceptualization; funding acquisition; investigation; methodology; supervision; visualization; writing – review and editing.

ACKNOWLEDGEMENTS

We thank the reviewers for their very useful and constructive comments, which have greatly helped in improving the quality of the presentation of our results. The simulations have been partly run at CINECA thanks to the computational resources made available through the ISCRA-C projects FEMTUF – HP10CTQ8X7 and FEM-GPU – HP10CQYKJ1 and through the EuroHPC JU Benchmark And Development project EHPC-BEN-2024B03-045. This work has been partly supported by the ESCAPE-2, European Union EXCELLENT SCIENCE - Future and Emerging Technologies (FET) programme (grant agreement no. 800897). We would also like to thank Dr Christian Kühnlein, Dr James Doyle, and Dr Saša Gaberšek for providing the data for the Terrain-Induced Rotor Experiment mountain wave.

DATA AVAILABILITY STATEMENT

Data will be made available upon reasonable request.

ORCID

Giuseppe Orlando https://orcid.org/0000-0002-7119-4231

Tommaso Benacchio https://orcid.org/0000-0002-0732-7167

Luca Bonaventura https://orcid.org/0000-0002-1994-0217

REFERENCES

Arndt, D., Bangerth, W., Bergbauer, M., Feder, M., Fehling, M., Heinz, J. et al. (2023) The deal.II library, Version 9.5. *Journal of Numerical Mathematics*, 31, 231–246.

Arnold, D., Brezzi, F., Cockburn, B. & Marini, L. (2002) Unified analysis of discontinuous Galerkin methods for elliptic problems. *SIAM journal on numerical analysis*, 39, 1749–1779.

Baldauf, M. & Pril, F. (2023) Further developments in the Discontinuous Galerkin based dynamical core for ICON (BRIDGE). 45th EWGLAM/30th SRNWP meeting.

Bangerth, W., Hartmann, R. & Kanschat, G. (2007) deal II: A general-purpose object-oriented finite element library. *ACM Transactions on Mathematical Software*, 33, 24–51.

Benard, P., Marki, A., Neytchev, P. & Prtenjak, M. (2000) Stabilization of nonlinear vertical diffusion schemes in the context of NWP models. *Monthly Weather Review*, 128, 1937–1948.

Blaise, S., Lambrechts, J. & Deleersnijder, E. (2016) A stabilization for three-dimensional discontinuous Galerkin discretizations applied to nonhydrostatic atmospheric simulations. *International Journal for Numerical Methods in Fluids*, 81, 558–585.

Bonaventura, L. (2000) A semi-implicit, semi-Lagrangian scheme using the height coordinate for a nonhydrostatic and fully elastic model of atmospheric flows. *Journal of Computational Physics*, 158, 186–213.

Bonaventura, L. & Ferretti, R. (2014) Semi-Lagrangian methods for parabolic problems in divergence form. *SIAM Journal of Scientific Computing*, 36, A2458–A2477.

Bramble, J., Kwak, D. & Pasciak, J. (1994) Uniform convergence of multigrid v-cycle iterations for indefinite and nonsymmetric problems. *SIAM journal on numerical analysis*, 31, 1746–1763.

Casulli, V. & Greenspan, D. (1984) Pressure method for the numerical solution of transient, compressible fluid flows. *International Journal for Numerical Methods in Fluids*, 4, 1001–1012.

Côté, J. (1997) Variable resolution techniques for weather prediction. *Meteorology and Atmospheric Physics*, 63, 31–38.

Daniels, M., Lundquist, K., Mirocha, J., Wiersema, D. & Chow, F.K. (2016) A new vertical grid nesting capability in the Weather Research and Forecasting (wrf) Model. *Monthly Weather Review*, 144, 3725–3747.

Davies, L. & Brown, A. (2001) Assessment of which scales of orography can be credibly resolved in a numerical model. *Quarterly Journal of the Royal Meteorological Society*, 127, 1225–1237.

Davies, T., Staniforth, A., Wood, N. & Thuburn, J. (2003) Validity of anelastic and other equation sets as inferred from normal-mode analysis. *Quarterly Journal of the Royal Meteorological Society*, 129, 2761–2775.

Dolejsi, V. (2024) Non-hydrostatic mesoscale atmospheric modeling by the anisotropic mesh adaptive discontinuous Galerkin method. Tech. Rep., arXiv:2401.10662.

Doyle, J., Durran, D., Chen, C., Colle, B., Georgelin, M., Grubisic, V. et al. (2000) An intercomparison of model-predicted wave breaking for the 11 January 1972 Boulder windstorm. *Monthly Weather Review*, 128, 901–914.

Doyle, J.D., Gaberšek, S., Jiang, Q., Bernardet, L., Brown, J., Dörnbrack, A. et al. (2011) An intercomparison of T-REX mountain-wave simulations and implications for mesoscale predictability. *Monthly Weather Review*, 139, 2811–2831.

Du, Q., Wang, D. & Zhu, L. (2009) On mesh geometry and stiffness matrix conditioning for general finite element spaces. *SIAM journal on numerical analysis*, 47, 1421–1444.

Düben, P. & Korn, P. (2014) Atmosphere and ocean modeling on grids of variable resolution—a 2D case study. *Monthly Weather Review*, 142, 1997–2017.

Dumbser, M. & Casulli, V. (2016) A conservative, weakly nonlinear semi-implicit finite volume scheme for the compressible Navier-Stokes equations with general equation of state. *Applied Mathematics and Computation*, 272, 479–497.

Esmaily, M., Jofre, L., Mani, A. & Iaccarino, G. (2018) A scalable geometric multigrid solver for nonsymmetric elliptic systems with application to variable-density flows. *Journal of Computational Physics*, 357, 142–158.

Fahs, H. (2015) High-order discontinuous Galerkin method for time-domain electromagnetics on non-conforming hybrid meshes. *Mathematics and Computers in Simulation*, 107, 134–156.

Fritts, D., Lund, A., Lund, T. & Yudin, V. (2022) Impacts of limited model resolution on the representation of mountain wave and secondary gravity wave dynamics in local and global models. 1: Mountain waves in the stratosphere and mesosphere. *Journal of Geophysical Research: Atmospheres*, 127, e2021JD035990.

Gal-Chen, T. & Somerville, R. (1975) On the use of a coordinate transformation for the solution of the Navier-Stokes equations. *Journal of Computational Physics*, 17, 209–228.

Giraldo, F. (2020) *An Introduction to Element-Based Galerkin Methods on Tensor-Product Bases*. Cham: Springer Nature Switzerland.

Giraldo, F., Kelly, J. & Constantinescu, E. (2013) Implicit-explicit formulations of a three-dimensional nonhydrostatic unified model of the atmosphere (NUMA). *SIAM Journal of Scientific Computing*, 35, 1162–1194.

Giraldo, F. & Restelli, M. (2008) A study of spectral element and discontinuous Galerkin methods for the Navier-Stokes equations in nonhydrostatic mesoscale atmospheric modeling: Equation sets and test cases. *Journal of Computational Physics*, 227, 3849–3877.

Girard, C. & Delage, Y. (1990) Stable schemes for nonlinear vertical diffusion in atmospheric circulation models. *Monthly Weather Review*, 118, 737–745.

Harrison, E. & Elsberry, R. (1972) A method for incorporating nested finite grids in the solution of systems of geophysical equations. *Journal of the Atmospheric Sciences*, 29, 1235–1245.

Heinz, J., Munch, P. & Kaltenbacher, M. (2023) High-order non-conforming discontinuous Galerkin methods for the acoustic conservation equations. *International Journal for Numerical Methods in Engineering*, 124, 2034–2049.

Hellsten, A., Ketelsen, K., Sühring, M., Auvinen, M., Maronga, B., Knigge, C. et al. (2021) A nested multi-scale system implemented in the large-eddy simulation model PALM model system 6.0. *Geoscientific Model Development*, 14, 3185–3214.

Hosea, M. & Shampine, L. (1996) Analysis and implementation of TR-BDF2. *Applied Numerical Mathematics*, 20, 21–37.

Jablonowski, C., Oehmke, R. & Stout, Q. (2009) Block-structured adaptive meshes and reduced grids for atmospheric general circulation models. *Philosophical Transactions of the Royal Society A: Mathematical, Physical and Engineering Sciences*, 367, 4497–4522.

Kamenski, L., Huang, W. & Xu, H. (2014) Conditioning of finite element equations with arbitrary anisotropic meshes. *Mathematics of computation*, 83, 2187–2211.

Kanehama, T., Sandu, I., Beljaars, A., van Niekerk, A. & Lott, F. (2019) Which orographic scales matter most for medium-range forecast skill in the Northern Hemisphere winter? *Journal of Advances in Modeling Earth Systems*, 11, 3893–3910.

Klemp, J. & Durran, D. (1983) An upper boundary condition permitting internal gravity wave radiation in numerical mesoscale models. *Monthly Weather Review*, 111, 430–444.

Klemp, J. & Lilly, D. (1978) Numerical simulation of hydrostatic mountain waves. *Journal of the Atmospheric Sciences*, 35, 78–107.

Kopera, M. & Giraldo, F. (2014) Analysis of adaptive mesh refinement for IMEX Discontinuous Galerkin solutions of the compressible Euler equations with application to atmospheric simulations. *Journal of Computational Physics*, 275, 92–117.

Kühnlein, C., Dörnbrack, A. & Weissmann, M. (2013) High-resolution Doppler LIDAR observations of transient downslope flows and rotors. *Monthly weather review*, 141, 3257–3272.

Li, J., Fang, F., Steppeler, J., Zhu, J., Cheng, Y. & Wu, X. (2021) Demonstration of a three-dimensional dynamically adaptive atmospheric dynamic framework for the simulation of mountain waves. *Meteorology and Atmospheric Physics*, 133, 1627–1645.

Lindzen, R. & Fox-Rabinovitz, M. (1989) Consistent vertical and horizontal resolution. *Monthly Weather Review*, 117, 2575–2583.

Long, D. & Thuburn, J. (2011) Numerical wave propagation on non-uniform one-dimensional staggered grids. *Journal of Computational Physics*, 230, 2643–2659.

Louis, J. (1979) A parametric model of vertical eddy fluxes in the atmosphere. *Boundary Layer Meteorology*, 17, 197–202.

Maffre, P., Ladant, J., Donnadieu, Y., Sepulchre, P. & Goddéris, Y. (2018) The influence of orography on modern ocean circulation. *Climate Dynamics*, 50, 1277–1289.

Mahalov, A. & Moustaoui, M. (2009) Vertically nested nonhydrostatic model for multiscale resolution of flows in the upper troposphere and lower stratosphere. *Journal of Computational Physics*, 228, 1294–1311.

McFarlane, N. (1987) The effect of orographically excited gravity wave drag on the general circulation of the lower stratosphere and troposphere. *Journal of the Atmospheric Sciences*, 44, 1775–1800.

McTaggart-Cowan, R., Girard, C., Plante, A. & Desgagné, M. (2011) The utility of upper-boundary nesting in NWP. *Monthly Weather Review*, 139, 2117–2144.

Melvin, T., Benacchio, T., Shipway, B., Wood, N., Thuburn, J. & Cotter, C. (2019) A mixed finite-element, finite-volume, semi-implicit discretization for atmospheric dynamics: Cartesian geometry. *Quarterly Journal of the Royal Meteorological Society*, 145, 2835–2853.

Miller, M., Palmer, T. & Swinbank, R. (1989) Parametrization and influence of subgridscale orography in general circulation and numerical weather prediction models. *Meteorology and Atmospheric Physics*, 40, 84–109.

Mirocha, J. & Lundquist, K. (2017) Assessment of vertical mesh refinement in concurrently nested large-eddy simulations using the Weather Research and Forecasting Model. *Monthly Weather Review*, 145, 3025–3048.

Müller, A., Behrens, J., Giraldo, F. & Wirth, V. (2013) Comparison between adaptive and uniform Discontinuous Galerkin simulations in dry 2D bubble experiments. *Journal of Computational Physics*, 235, 371–393.

Orlando, G. (2023) *Modelling and Simulations of Two-Phase Flows Including Geometric Variables*. Ph.D. thesis, Milano: Politecnico di Milano. Available from: http://hdl.handle.net/10589/198599

Orlando, G., Barbante, P. & Bonaventura, L. (2022) An efficient IMEX-DG solver for the compressible Navier-Stokes equations for non-ideal gases. *Journal of Computational Physics*, 471, 111653.

Orlando, G., Benacchio, T. & Bonaventura, L. (2023) An IMEX-DG solver for atmospheric dynamics simulations with adaptive mesh refinement. *Journal of Computational and Applied Mathematics*, 427, 115124.

Orlando, G., Benacchio, T. & Bonaventura, L. (2024) Impact of Curved Elements for Flows Over orography with a Discontinuous Galerkin Scheme. https://arxiv.org/abs/2404.09319

Palmer, T., Shutts, G. & Swinbank, R. (1986) Alleviation of a systematic westerly bias in general circulation and numerical weather prediction models through an orographic gravity wave drag parametrization. *Quarterly Journal of the Royal Meteorological Society*, 112, 1001–1039.

Phillips, N. & Shukla, J. (1973) On the strategy of combining coarse and fine grid meshes in numerical weather prediction. *Journal of Applied Meteorology and Climatology*, 12, 763–770.

Pinty, J., Benoit, R., Richard, E. & Laprise, R. (1995) Simple tests of a semi-implicit semi-Lagrangian model on 2D mountain wave problems. *Monthly Weather Review*, 123, 3042–3058.

Prusa, J. & Smolarkiewicz, P. (2003) An all-scale anelastic model for geophysical flows: Dynamic grid deformation. *Journal of Computational Physics*, 190, 601–622.

Restelli, M. (2007) *Semi-Lagrangian and Semi-Implicit Discontinuous Galerkin Methods for Atmospheric Modeling Applications*. Ph.D. thesis, Milano: Politecnico di Milano.

Sandu, I., van Niekerk, A., Shepherd, T., Vosper, S., Zadra, A., Bacmeister, J. et al. (2019) Impacts of orography on large-scale atmospheric circulation. *Nature Climate and Atmospheric Science*, 2, 10.

Skamarock, W. & Klemp, J. (1993) Adaptive grid refinement for two-dimensional and three-dimensional nonhydrostatic atmospheric flow. *Monthly Weather Review*, 121, 788–804.

Skamarock, W., Klemp, J., Duda, M., Fowler, L., Park, S.-H. & Ringler, T. (2012) A multiscale nonhydrostatic atmospheric model using centroidal Voronoi tesselations and C-grid staggering. *Monthly Weather Review*, 140, 3090–3105.

Skamarock, W., Klemp, J., Dudhia, J., Gill, D., Liu, Z., Berner, J. et al. (2021) A description of the advanced research WRF model version 4.3. Tech. rep., NCAR, NCAR/TN-556+ STR.

Skamarock, W., Oliger, J. & Street, R. (1989) Adaptive grid refinement for numerical weather prediction. *Journal of Computational Physics*, 80, 27–60.

Skamarock, W., Snyder, C., Klemp, J. & Park, S. (2019) Vertical resolution requirements in atmospheric simulation. *Monthly Weather Review*, 147, 2641–2656.

Smith, R. (1979) The influence of mountains on the atmosphere. *Advances in Geophysics*, 21, 87–230.

Staniforth, A. (2022) *Global Atmospheric and Oceanic Modelling: Fundamental Equations*. Cambridge, UK: Cambridge University Press.

Staniforth, A. & White, A. (2019) Forms of the thermodynamic energy equation for moist air. *Quarterly Journal of the Royal Meteorological Society*, 145, 386–393.

Steppeler, J., Hess, R., Doms, G., Schättler, U. & Bonaventura, L. (2003) Review of numerical methods for nonhydrostatic weather prediction models. *Meteorology and Atmospheric Physics*, 82, 287–301.

Tang, Y., Lean, H. & Bornemann, J. (2013) The benefits of the Met Office variable resolution NWP model for forecasting convection. *Meteorological Applications*, 20, 417–426.

Tissaoui, Y., Marras, S., Quaini, A., de Brangaca Alves, F. & Giraldo, F. (2023) A non-column based, fully unstructured implementation of Kessler's microphysics with warm rain using continuous and discontinuous spectral elements. *Journal of Advances in Modeling Earth Systems*, 15, e2022MS003283.

Tumolo, G. & Bonaventura, L. (2015) A semi-implicit, semi-Lagrangian discontinuous Galerkin framework for adaptive numerical weather prediction. *Quarterly Journal of the Royal Meteorological Society*, 141, 2582–2601.

Vichnevetsky, R. (1987) Wave propagation and reflection in irregular grids for hyperbolic equations. *Applied Numerical Mathematics*, 3, 133–166.

Weller, H. (2009) Predicting mesh density for adaptive modelling of the global atmosphere. *Philosophical Transactions of the Royal Society A: Mathematical, Physical and Engineering Sciences*, 367, 4523–4542.

Yelash, L., Müller, A., Lukáčová-Medvid'ová, M., Giraldo, F. & Wirth, V. (2014) Adaptive discontinuous evolution Galerkin method for dry atmospheric flow. *Journal of Computational Physics*, 268, 106–133.

Zhang, D., Chang, H., Seaman, N., Warner, T. & Fritsch, J. (1986) A two-way interactive nesting procedure with variable terrain resolution. *Monthly Weather Review*, 114, 1330–1339.

How to cite this article: Orlando, G., Benacchio, T. & Bonaventura, L. (2024) Robust and accurate simulations of flows over orography using non-conforming meshes. *Quarterly Journal of the Royal Meteorological Society*, 150(765), 4750–4770. Available from: https://doi.org/10.1002/qj.4839